Maintenance of Tropical Intraseasonal Variability: Impact of Evaporation–Wind Feedback and Midlatitude Storms

JOHNNY WEI-BING LIN

Department of Atmospheric Sciences, University of California, Los Angeles, Los Angeles, California

J. DAVID NEELIN AND NING ZENG

Department of Atmospheric Sciences and Institute of Geophysics and Planetary Physics, University of California, Los Angeles, Los Angeles, California

(Manuscript received 24 June 1998, in final form 8 September 1999)

ABSTRACT

An intraseasonal tropical oscillation with a period of 20–80 days is simulated in the Neelin–Zeng Quasi-Equilibrium Tropical Circulation Model. This model is an intermediate-level atmospheric model that includes primitive equation nonlinearity, radiative–convective feedbacks, a simple land model with soil moisture, and a Betts–Miller-type moist convective adjustment parameterization. Vertical temperature and moisture structures in the model are based on quasi-equilibrium profiles taken from deep convective regions. The tropical intraseasonal variability is reasonably broadband. The eastward propagating 20–80-day variability is dominated by zonal wavenumber 1, shows features similar to an irregular Madden–Julian oscillation (MJO), and exhibits amplitude and phase speeds that vary both seasonally and between events. At higher wavenumbers, the model has a distinction between the low-frequency MJO-like band and the moist Kelvin wave band, similar to that found in observations. In the model, it is conjectured that this arises by interaction of the wavenumber-1 moist Kelvin wave with the zonally asymmetric basic state.

Experiments using climatological sea surface temperature forcing are conducted using this model to examine the effects of evaporation–wind feedback and extratropical excitation on the maintenance of intraseasonal variability, with particular attention paid to the low wavenumber mode in the 20–80-day band. These experiments indicate that evaporation–wind feedback partially organizes this intraseasonal variability by reducing damping, but it is not by itself sufficient to sustain this oscillation for the most realistic parameters. Excitation by extratropical variability is a major source of energy for the intraseasonal variability in this model. When midlatitude storms are suppressed, tropical intraseasonal variability is nearly eliminated. However, the eastward propagating intraseasonal signal appears most clearly when midlatitude excitation is aided by the evaporation–wind feedback.

1. Introduction

a. Overview

The Madden–Julian oscillation (MJO), first recognized by Madden and Julian (1971, 1972), is an eastward-propagating tropical intraseasonal oscillation that is evident in a number of atmospheric fields, including zonal wind speed and outgoing longwave radiation (OLR). In some fields (such as upper-level zonal wind), the propagation is global in extent, while in others, the propagation is confined to a specific region. For instance, the signal in OLR is generally confined to the Indian and western Pacific Oceans. The MJO has a period between 30 and 60 days, with wavenumber-1–3 structure. The phase speed of the MJO is approximately 5 m s^{-1} for convection and 10 m s^{-1} in upper-level winds (e.g., Hendon and Salby 1994). Variability in upper- and lower-level wind fields also appear out of phase with each other. Descriptions of these and other features of the MJO are found in a variety of observational studies. These include compositing studies (e.g., Knutson and Weickmann 1987; Hendon and Salby 1994) and studies of individual MJO events (e.g., Hsu et al. 1990). Other observational studies focus on specific features of the MJO such as surface pressure (e.g., Milliff and Madden 1996), convection (e.g., Gruber 1974; Murakami 1984; Weickmann et al. 1985; Lau and Chan 1985; Wang and Rui 1990; Hendon and Liebmann 1994; Jones and Weare 1996; Zhang and Hendon 1997), and the planetary circulation (e.g.,

Corresponding author address: J. David Neelin, Department of Atmospheric Sciences, University of California, Los Angeles, Los Angeles, CA 90095-1565.
E-mail: neelin@atmos.ucla.edu

Weickmann et al. 1985; Hayashi and Golder 1986). Madden and Julian (1994) provide a review of observational work on the MJO.

b. Previously proposed MJO maintenance mechanisms

Because of its eastward-propagating, low-frequency structure, early work characterized the MJO as a Kelvin-like mode of low wavenumber, since Kelvin waves also propagate eastward and have a dominant signal in zonal wind, with a maximum on the equator (Lindzen 1974; Chang 1977). While equatorial Kelvin wave theory for dry dynamics predicts phase speeds of 30–60 m s^{-1} for the first baroclinic mode, when interactions between convection and large-scale dynamics are taken into account, slower (though in general still slightly faster than observed) phase speeds are obtained in Kelvin wave MJO models (e.g., Hayashi and Sumi 1986; Lau and Peng 1987; Swinbank et al. 1988; Chang and Lim 1988; Lau et al. 1988). Many of these models incorporated this interaction through the conditional instability of the second kind (CISK) instability mechanism, which hypothesizes that low-level moisture convergence and latent heat release feed off of one another to create atmospheric instability at large scales (Charney and Eliassen 1964; Ooyama 1964; Hayashi 1971; Lindzen 1974). As a result, the MJO was interpreted as a mode of the tropical atmosphere with CISK instability.

The instability aspect of CISK has recently been called into question (e.g., Emanuel et al. 1994), largely because of the modest size of the moist available energy in the tropical atmosphere (Randall and Wang 1992). However, the spatial structure and phase speed considerations of the MJO are separable from questions of large-scale atmospheric instability. For instance, analytical work by Neelin and Yu (1994) suggests that for a moist atmosphere under Betts–Miller (1986) moist convective adjustment, the MJO is described by a Kelvin-like mode whose slow phase speed is set by the gross moist stability. The spatial structure and phase speed concurs with CISK models, but there is no CISK in the sense of instability. The term ''convective interaction with dynamics'' (CID) was suggested as a means of referring to such interactions without assuming instability (Neelin and Yu 1994). As long as the ensemble effects of convection strongly influence the large scale, an MJO-like mode with slow phase speed will exist even in the absence of CISK instability.

Although moist Kelvin wave theory appears to describe certain aspects of the observed MJO, including its form and slower-than-dry-dynamics phase speed, there is still uncertainty as to whether to consider the MJO as a moist Kelvin wave or as something different altogether. Observational work done by Hendon and Salby (1994) suggests that the circulation component of the MJO has a forced response component that has the form of a Rossby–Kelvin wave coupled to convection. Other observational studies of tropical OLR have shown the existence of Kelvin-like waves associated with convection (Takayabu 1994; Dunkerton and Crum 1995). Some work suggests that these waves move with phase speeds different from the MJO (Dunkerton and Crum 1995). Analysis of OLR and deep-layer temperature data by Wheeler and Kiladis (1999, hereafter WK) suggests that while both moist Kelvin waves and the MJO appear to be ''convectively coupled'' equatorial waves, the spectral peaks as a function of wavenumber and frequency are more complex. A feature corresponding to the dispersion curve of a moist phase speed Kelvin wave coexists with a low-frequency (30–60 day) feature that extends as far as wavenumber 6. Wheeler and Kiladis interpret these as separate entities, although we note that at wavenumber 1, which has most of the power, the two curves are not clearly distinguished. The model used in the present study has analogs of both aspects. For a discussion that applies to both in the model, we use the term ''moist-Kelvin/MJO-like'' variance (without assuming they are necessarily linked). ''Intraseasonal variance'' refers to this and other intraseasonal variability collectively.

Besides the wave identity of the MJO, there is also debate over what maintenance mechanism(s) act to maintain the oscillation against damping. The different mechanisms that have been proposed to explain MJO maintenance fall into the following general types:

1) Instability associated with released convective available potential energy (CAPE) at large scales,
2) Evaporation–wind feedback (EWF),
3) Midlatitude excitation in the troposphere,
4) Stochastic convective variance, and
5) Other oscillatory heat sources.

In the first proposed maintenance mechanism, it is suggested that CISK-type instability provides the energy needed to maintain the oscillation (e.g., Lau and Peng 1987; Chang and Lim 1988), which implies conversion of CAPE to large-scale motions. However, there is debate as to whether CISK-type instability can really exist. Some observations suggest that rather than exhibiting high levels of large-scale convective instability, lower-tropospheric convective regions are actually near neutral with respect to adiabatic motion (Betts 1982; Emanuel 1988; Xu and Emanuel 1989). Lim et al. (1990) and Crum and Dunkerton (1992) note that because linear wave–CISK theory predicts increasing growth with increasing wavenumber, such a flow field will eventually be overwhelmed by the smallest scales in the system; this is not found in observations, which are dominated by planetary-scale features. Nonlinear wave–CISK theory may provide ways to circumvent this problem (e.g., Lau and Peng 1987; Hendon 1988; Lim et al. 1990), but the upward motions still tend to occur at the smallest available scales. Salby et al. (1994) suggest that ''frictional'' wave–CISK, where frictional damping in the boundary

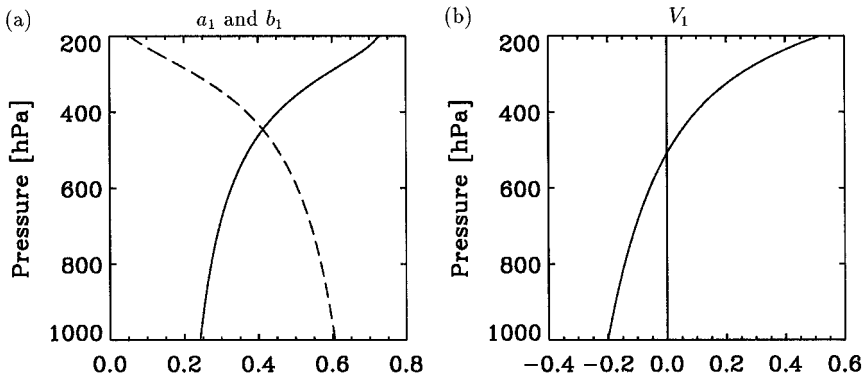

FIG. 1. Vertical profiles of basis functions for (a) temperature a_1 (solid) and humidity b_1 (dashed) and (b) baroclinic component of horizontal velocity V_1.

layer interacts with convergence associated with a Kelvin wave, preferentially selects motion at larger scales, in contrast with linear wave–CISK theory. Bladé and Hartmann (1993) examined a parameter regime in which CISK instability occurs in part of the domain while the rest of the domain is marginally stable. Random fluctuations (from midlatitudes) set off a stationary growth phase that subsequently propagates eastward and decays. They underline the recharge time needed for the CISK instability in this regime.

Another possible method of providing variance to the MJO is the evaporation–wind feedback (EWF) mechanism (also known as ''wind-induced, surface heat exchange'' or WISHE). Emanuel (1987) and Neelin et al. (1987) first described the mechanism in a linear formulation, while Xie et al. (1993) presented a quasilinear extension. In the EWF theory, eastward propagation of convective regions is driven by anomalies in evaporation induced east of the convective regions by the rise of anomalous surface winds east of the convective regions. In the simplest formulation, the anomalies of evaporation are induced by convectively driven low-level convergence, superimposed on top of mean easterlies, such that evaporation is enhanced east of the enhanced convection and suppressed west of the enhanced convection. Linear perturbation analysis (Neelin and Yu 1994) as well as general circulation model (GCM) and other model experiments (e.g., Numaguti and Hayashi 1991; Seager and Zebiak 1994; Crum and Dunkerton 1994; Hayashi and Golder 1997) suggest that the EWF can tend to maintain the MJO. However, beginning with Wang (1988), several studies have voiced doubts over the role of the EWF in observations. Analysis of the European Centre for Medium-Range Weather Forecasts (ECMWF) analyses in the warm pool region (Jones and Weare 1996; Hendon and Glick 1997), where mean wind is both easterly and westerly, suggest an evaporation–convection lag relationship that is not in phase with one that is implied by the simplest EWF theory for the basic Kelvin wave solution with homogeneous boundary conditions and mean easterlies. Sperber et al.'s (1997) analysis of the National Centers for Environmental Prediction (NCEP) reanalyses also questions the role of the EWF in maintaining the MJO. However, the plots in Sperber et al. (1997) suggest an association of evaporation and planetary boundary layer (PBL) moist static energy that might be quite compatible with the EWF. Clearly, more sophisticated theory is needed to guide observational tests.

Various studies also suggest that the extratropics may influence tropical intraseasonal variance. Liebmann and Hartmann's (1984) midlatitude–Tropics wintertime correlation study suggests tropospheric midlatitude influence on tropical intraseasonal variability. Analysis by Hsu et al. (1990) of the tropical intraseasonal variability during 1985–86 suggests that these events were initiated by subtropical Rossby wave rains. Ferranti et al.'s (1990) tests with the ECMWF model also indicate a link in both directions between the extratropics and Tropics in that constraining one toward observed states improves forecasts in the other. Complex empirical orthogonal function (EOF) analysis by Anyamba and Weare (1995) suggests that some of the OLR anomalies associated with the MJO have origins in the extratropics. The analysis by Slingo et al. (1996) of intraseasonal variability in 15 atmospheric GCMs suggests that accurate simulation of intraseasonal variability may require accurate simulation of interactions between the Tropics and midlatitudes. Meehl et al. (1996) analyzed analysis products and Tropical Ocean Global Atmosphere Coupled Ocean–Atmosphere Response Experiment (TOGA COARE) data to conclude that MJO Indian Ocean convective activity is connected to a downstream wave train through the midlatitudes. Slingo (1998) examined the influence of extratropical effects on tropical convection and wave activity on shorter timescales. Yanai et al.'s (2000) study of TOGA COARE intensive observing period (IOP) perturbation kinetic energy (PKE) budgets also suggests MJO interaction with midlatitudes.

Stochastic convective forcing has also been suggested as a possible source of variance for maintaining the

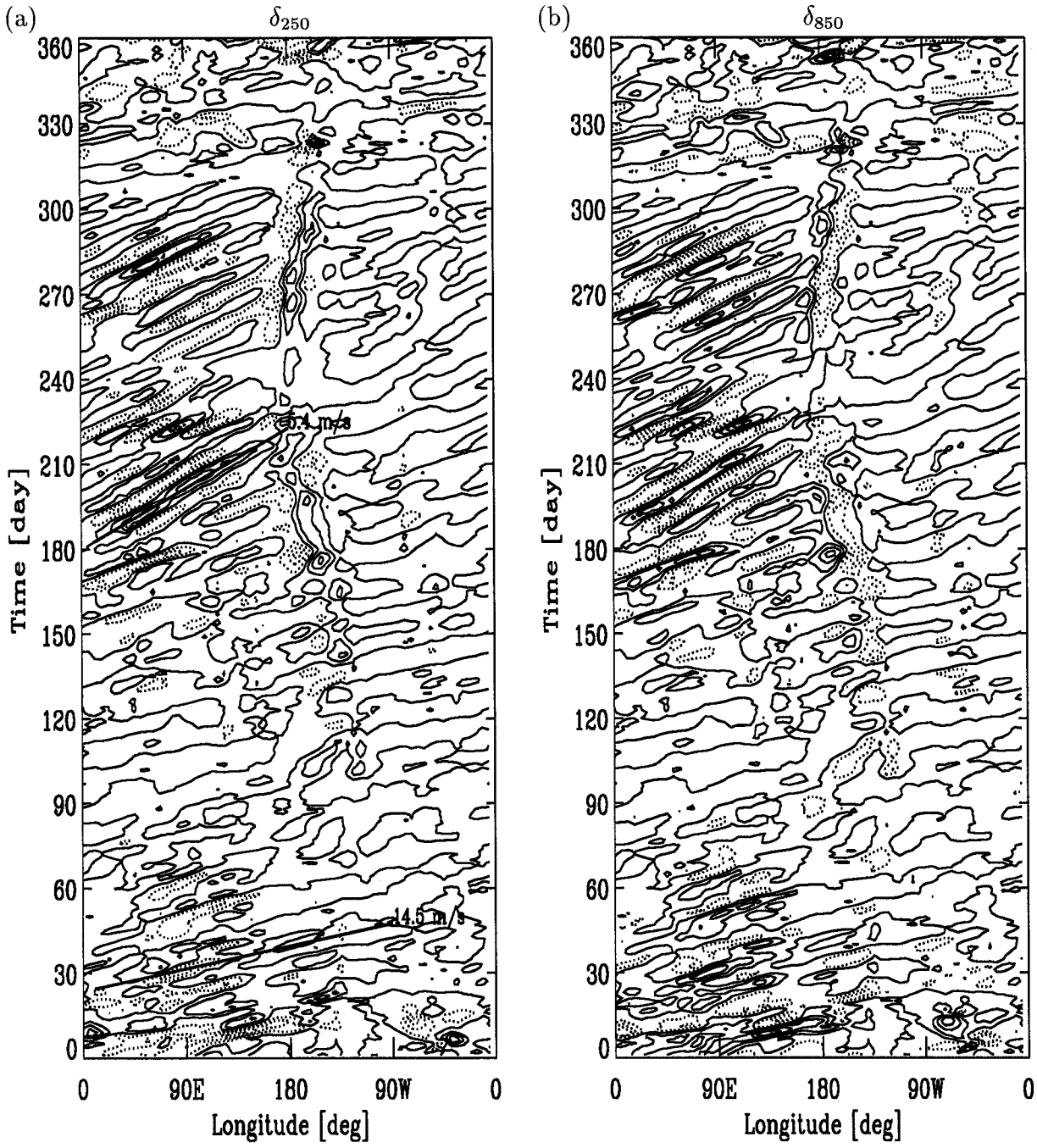

FIG. 2. Time–longitude plots of equatorial (nonareally weighted spatial mean from 7.5°S to 7.5°N) daily mean anomalies of divergence at (a) 250 hPa (contour 5×10^{-7} s^{-1}) and (b) 850 hPa (contour 2×10^{-7} s^{-1}) for the control run. Negative anomalies are dotted. Day 1 begins with the second year of the model run; the first year is discarded because of spinup. Jan–Dec is shown. Approximate phase speed lines for δ_{250} are drawn for summer (5.4 m s^{-1}) and winter (14.5 m s^{-1}) events.

MJO. GCM studies of tropical intraseasonal variance use cumulus parameterizations that simulate the mean effects of subgrid convection but do not explicitly model the subgrid convective variance (such as those associated with mesoscale systems). However, there are indications that such small-scale effects could feed back onto the large scale. Salby and Garcia (1987) found that a stochastic convective heating source with seasonal variability included could produce a Kelvin wave that shows similarities to the observed MJO. Model results by Yu and Neelin (1994) using ''white noise'' thermal forcing (to simulate subgrid convective variance) shows

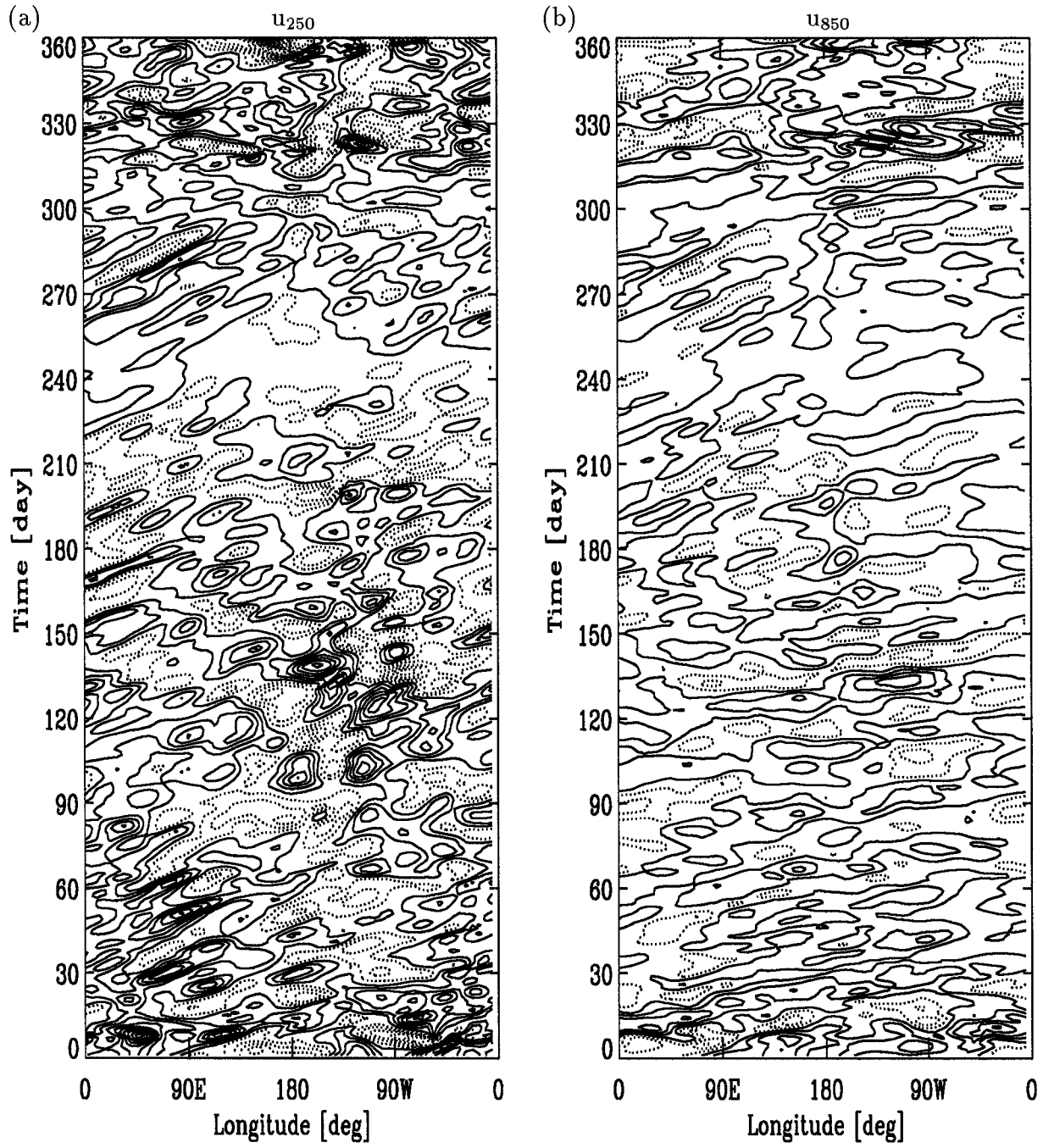

FIG. 3. As in Fig. 2, except zonal wind anomalies at (a) 250 hPa (contour 1 m s^{-1}) and (b) 850 hPa (contour 0.5 m s^{-1}) for the control run are shown.

feedback of spectral power onto low-frequency, low-wavenumber modes, which suggests that stochastic convective forcing might also help maintain the MJO mode.

Following the early work by Matsuno (1966) [and later Gill (1980)], studies have been conducted that assume a Kelvin-like MJO circulation is maintained by an oscillating heat source (e.g., Chang 1977; Hayashi and Miyahara 1987; Itoh and Nishi 1990). As of yet, such a heating source has not yet been concretely identified; Hu and Randall (1994) have suggested that such a heating source may be ''self-excited'' through nonlinear interactions between radiation, convection, and surface heat fluxes, although Brown and Bretherton (1995) did not find this mechanism to operate in their own model.

In addition, recent work has included modifications

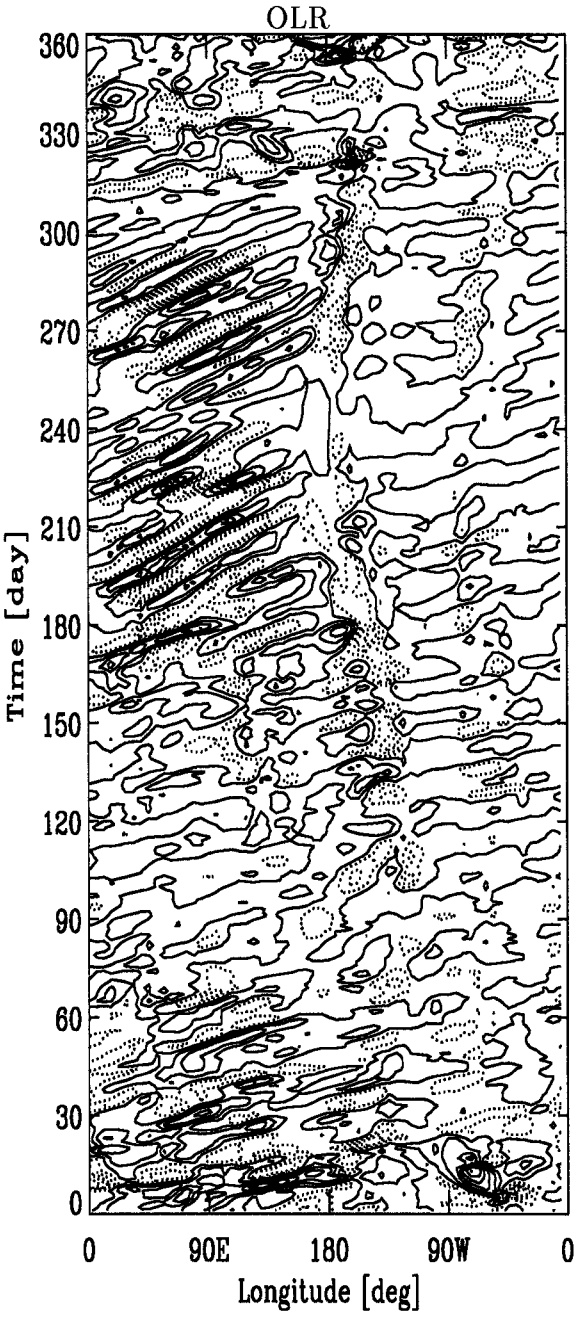

FIG. 4. As in Fig. 2, except OLR anomaly (contour 5 W m^{-2}) is shown for the control run.

to both propagation and maintenance of the MJO due to interaction with SST (Wang and Xie 1998; Waliser et al. 1999).

c. The focus of this study

This study analyzes the behavior of a low wavenumber, 20–80-day eastward-propagating feature in an intermediate-level atmospheric model. This broadband variability has features suggestive of both moist Kelvin wave variability and the MJO, as outlined in section 3b. Accordingly, this study also examines some of the proposed maintenance mechanisms for intraseasonal oscillations and their effects upon the moist-Kelvin/MJO-like feature produced by the model. Specifically, the EWF mechanism and the influence of tropospheric extratropical excitation are investigated. Although the EWF mechanism has been examined by a variety of other models, including GCMs, this paper presents a self-consistent modeling study of the relative importance of each of these mechanisms in maintaining moist-Kelvin/MJO-like variance using a model of moderately realistic complexity. In particular, this study presents a new way of testing the influence of extratropical excitation by suppressing baroclinic instability.

Section 2 describes the model used in this study. The moist-Kelvin/MJO-like feature simulated by the model is described in section 3. Tests of two proposed MJO maintenance mechanisms are discussed in section 4; sections 4a and 4b address the effects of the EWF and midlatitude excitation, respectively. A default hypothesis regarding the relationship between the moist-Kelvin wave and the MJO is presented in section 5. Discussion and conclusions are given in section 6. The model experiments described in this study suggest that both the EWF and tropospheric extratropical excitation play a role in maintaining intraseasonal variance. Of the two mechanisms, extratropical excitation provides the greater variance to the system in this model.

2. Model and analysis descriptions

The numerical modeling described in this paper uses the v1.0 (β release) of the Neelin–Zeng Quasi-Equilibrium Tropical Circulation Model (QTCM1). This model is a primitive, equation-based, intermediate-level atmospheric model that focuses on simulating the tropical atmosphere. Being more complicated than a simple model, the model has full nonlinearity and includes a radiative–convective feedback package and a simple land–soil moisture routine (but does not include topography). For its convective parameterization, this model uses the Betts–Miller (1986) moist convective adjustment scheme, which is also used in some GCMs. Model formulation is described in Neelin and Zeng (2000, hereafter NZ) and model implementation is described in Zeng et al. (2000, hereafter ZNC). Although NZ is based upon v2.0 of QTCM1 and ZNC is based on QTCM1 v2.1, most of the key results for climatology and interannual variability also apply to the version used in this present study (v1.0). Differences are pointed out in the discussion.

QTCM1 differs from most full-scale GCMs primarily in how the vertical temperature, humidity, and velocity structure of the atmosphere is represented. First, instead of representing the vertical structure by finite-differenced levels, the model uses a Galerkin expansion in

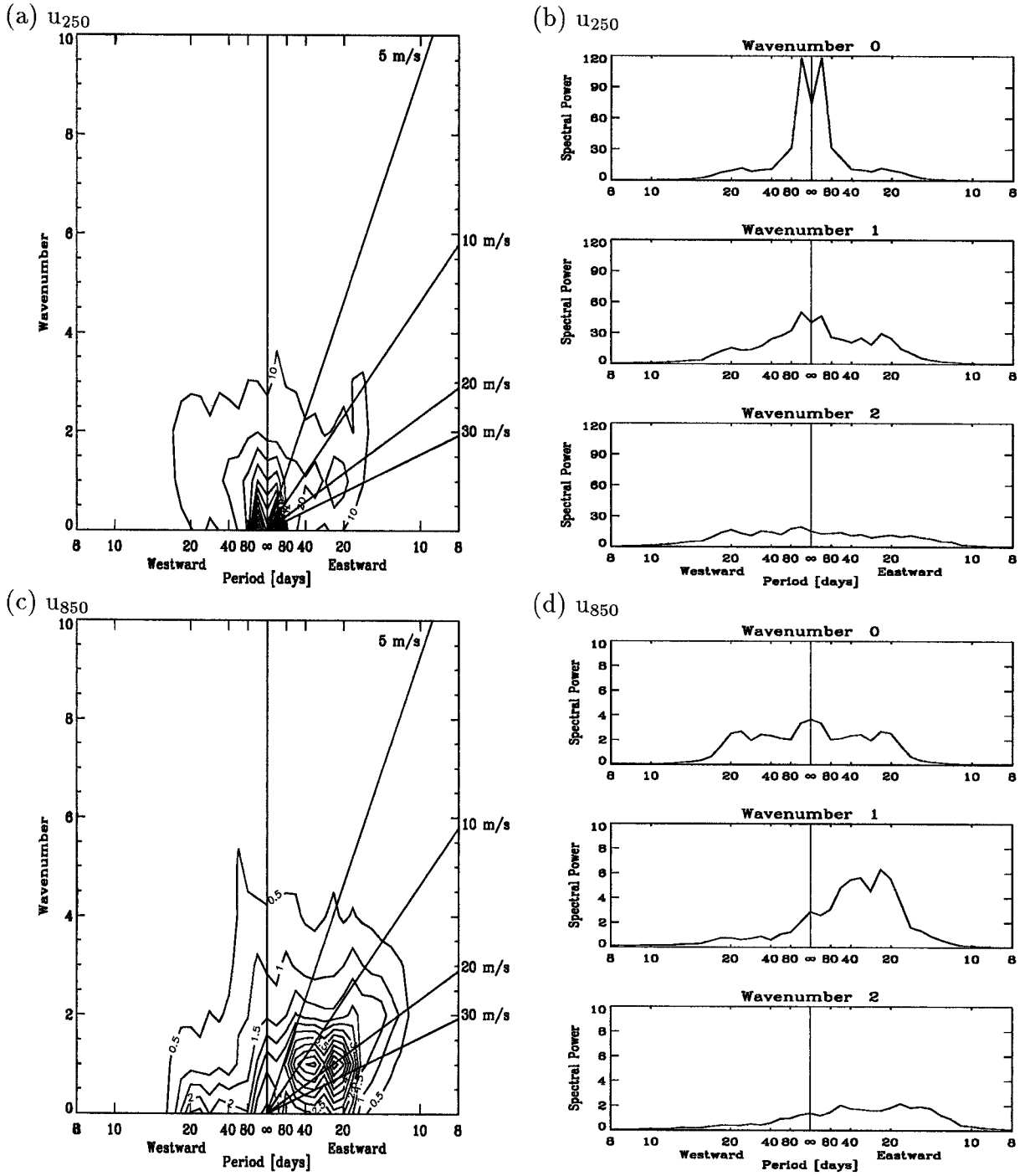

FIG. 5. Power spectral density (PSD) of equatorial (average 7.5°S–7.5°N) daily mean anomalies of (a) and (b) 250-hPa zonal wind; (c) and (d) 850-hPa zonal wind for the control run. PSD as (a) and (c) wavenumber–frequency contour plots; (b) and (d) wavenumber 0–2 slices are shown. Units of $(\text{m s}^{-1})^2$. Contour intervals are (a) 10 and (c) 0.5. Standard deviation of PSDs is 10%. See text for details regarding calculations of PSDs.

the vertical. The vertical basis functions are chosen according to analytical solutions under convective quasi-equilibrium conditions, so only a few need be retained. Temperature and humidity are each described by separate vertical basis functions (a_1 and b_1, respectively). Low-level variations in the humidity basis are larger than in the temperature basis. For velocity, QTCM1 uses a single baroclinic basis function (V_1), defined consistently with the temperature basis function, as well as a barotropic velocity mode (V_0). The vertical profiles of

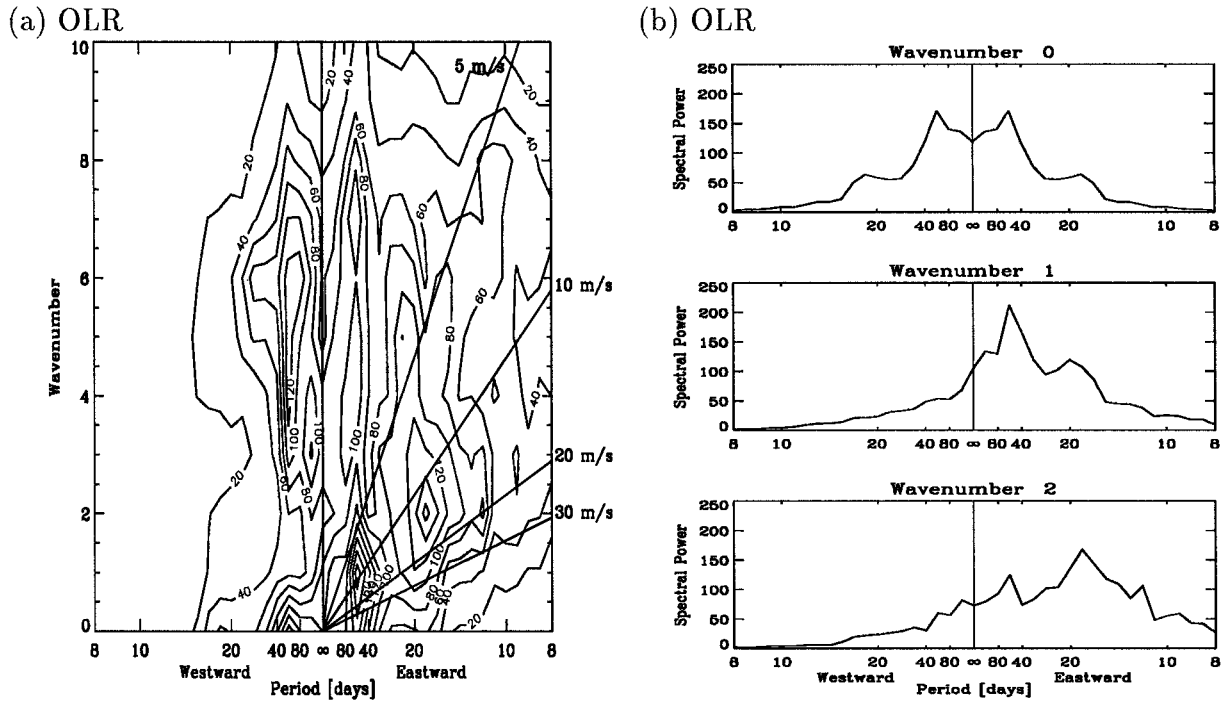

FIG. 6. PSD of equatorial (average 7.5°S–7.5°N) daily mean anomalies of OLR for the control run. PSD as (a) wavenumber–frequency contour plot and (b) wavenumber 0–2 slices are shown. Units of $(W\ m^{-2})^2$. Contour interval for (a) is 20. Standard deviation of PSDs is 10%.

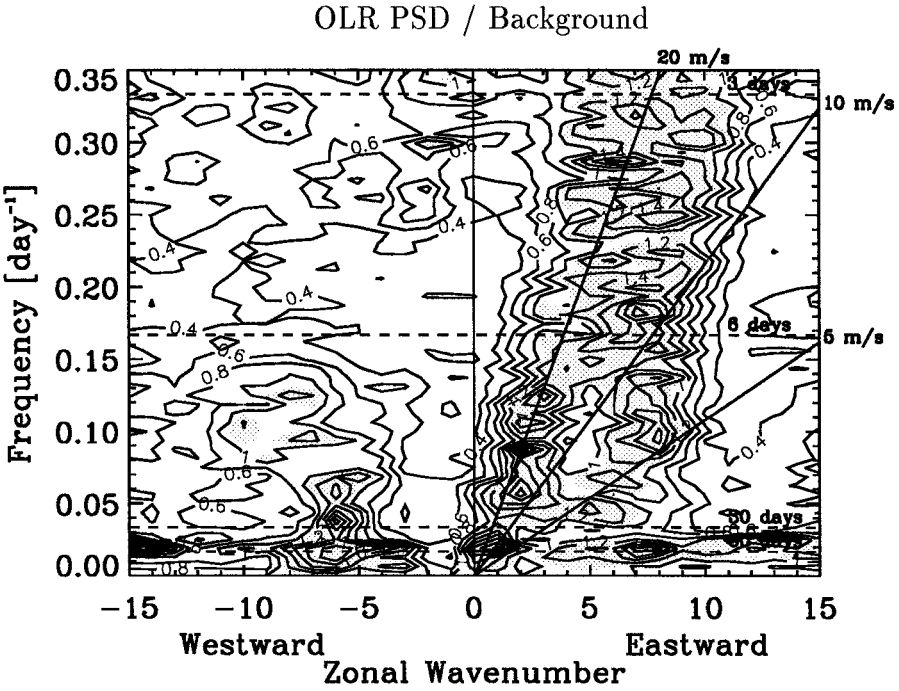

FIG. 7. PSD of equatorial (average 7.5°S–7.5°N) daily mean anomalies of OLR for the control run, normalized by an estimate of the background PSD. Contour interval is 0.2. Regions with values higher than 1.1 are shaded. Phase speed lines for 20, 10, and 5 m s^{-1} are shown.

a_1, b_1, and V_1 are given in Fig. 1. Currently, QTCM1 does not include a separate vertical degree of freedom describing the PBL.

These modes are chosen to accurately capture deep convective regions. Outside deep convective regions, the mode is simply a highly truncated Galerkin representation. The system is much more tightly constrained than a full-scale GCM yet hopefully retains the essential dynamics and nonlinear feedbacks. The result is that QTCM1 is easier to diagnose than a GCM and is computationally fast (about 8 min yr^{-1} on a Sun Ultra 2 workstation). Zeng et al. (2000) show results indicating that this intermediate-level model does a reasonable job simulating tropical climatology and ENSO variability.

Runs 46 yr in length (each year consisting of 12 30-day months) are conducted using climatological sea surface temperature (SST) as the lower boundary forcing. The SST used is from the Reynolds (1988) blended dataset. The first year of simulation is discarded to remove any residual spinup.

The time–longitude, spectral density, and spatial plots in this paper are based on anomalies that are calculated at each grid point by removing daily deviations (from daily means) from a spline fit to the monthly climatology over the 45-yr analysis period. No detrending is applied. For the lag-correlation maps (described in section 3), the anomalies used are based upon only the first 5 yr of the analysis period (daily mean data). The power spectral density (PSD) estimates described in this study use a Hanning window to control frequency leakage and the ''summing'' method (Press et al. 1989, 465–466), with a nonoverlapping bin group size of $K = 101$, to control the estimate error. Such binning yields a PSD standard deviation of 10%. Bandwidth for this bin group size is 0.006 23 day^{-1}. In the PSD plots, the lowest frequency that should be interpreted physically is thus 160 days. There is no binning in wavenumber. Wavenumber bandwidth is 1; wavenumber space is decomposed into integral wavenumbers.

3. Intraseasonal variability in QTCM1

a. Time–longitude evolution

The QTCM1 produces a number of interesting tropical features at an intraseasonal timescale. Figures 2 and 3 show time–longitude plots of equatorial (nonareally weighted spatial mean from 7.5°S to 7.5°N) daily mean upper- (250 hPa) and lower-level (850 hPa) divergence and zonal wind anomalies for a single year from the control run. Figure 4 shows the time–longitude plot for OLR anomalies. Eastward propagating intraseasonal signals are seen in these fields.

The nature of the signal differs depending on the field. Lower-level (850 hPa) zonal wind anomalies (Fig. 3b) show evidence of a globally propagating signal with phase speeds varying from a low of approximately 6 m s^{-1} during northern autumn to a high of about 20 m s^{-1} during northern spring. Additionally, during northern summer and autumn, the phase speeds vary longitudinally, with lower speeds (about 6 m s^{-1}) in the region of higher climatological convection from the Indian Ocean to Indonesia and the western Pacific (approximately 0°–180°) and higher speeds (about 12 m s^{-1}) from the eastern Pacific across to the Atlantic, where there is less climatological convection. During northern winter and spring, phase speeds appear constant across all longitudes.

In contrast, 250-hPa zonal wind anomalies (Fig. 3a) do not show an oscillation propagating to the same global extent. Northern winter anomalies begin around the Indian Ocean but are then stopped before they reach the date line. Besides sporadic eastward-propagating features such as these, much of the domain appears to be filled with less coherent variability. Although many examples can be found of 250-hPa zonal wind anomalies in anticorrelation with their 850-hPa counterparts, there are many cases where differing phase speeds appear to occur. Since the divergent part of the upper-level wind (Fig. 2a) is in clear anticorrelation with lower levels, this essentially indicates that other variability is also present. Faster phase speeds (>10 m s^{-1}) are more or less confined to November–January. Both the 850- and 250-hPa zonal wind anomalies are weakest in August and September.

The highest magnitudes of OLR anomalies (Fig. 4) occur over the Indian Ocean. The anomalies propagate eastward, stopping at around the date line, as is consistent with observations. Northern summer and autumn show the greatest activity. The signal during these seasons is also the most regular. The phase speed for the OLR anomaly ranges from approximately 5 to 10 m s^{-1}. Upper- and lower-level divergence anomalies (Fig. 2) mirror the OLR anomalies, with the appropriate phase shift of a half-cycle between 250 and 850 hPa.

The phase speeds calculated from the time–longitude plots can be compared to values calculated analytically from a linearization of the model analysis under a convective quasi-equilibrium approximation (Neelin and Yu 1994; Yu and Neelin 1994; Neelin 1997). In this analytical solution, the mean zonal wind is included, assuming slow meridional variation. Damping terms are neglected, so the baroclinic mode separates from the barotropic mode. EWF is also neglected. In this case, the phase speed c is set by the gross moist stability M_1, modified by advection:

$$c = \overline{u}_0 + \eta_a \overline{u}_1 + \left[\frac{\kappa M_1}{\hat{a}_1 + \hat{b}_1} + \eta_d^2 \overline{u}_1^2 \right]^{1/2} \qquad (1)$$

where

$$\eta_a = \frac{1}{2}\left[\frac{\langle V_1^3 \rangle}{\langle V_1^2 \rangle} + \frac{\langle a_1 V_1 \rangle + \langle b_1 V_1 \rangle}{\hat{a}_1 + \hat{b}_1} \right]$$

$$\eta_d = \frac{1}{2}\left[\frac{\langle V_1^3 \rangle}{\langle V_1^2 \rangle} - \frac{\langle a_1 V_1 \rangle + \langle b_1 V_1 \rangle}{\hat{a}_1 + \hat{b}_1} \right].$$

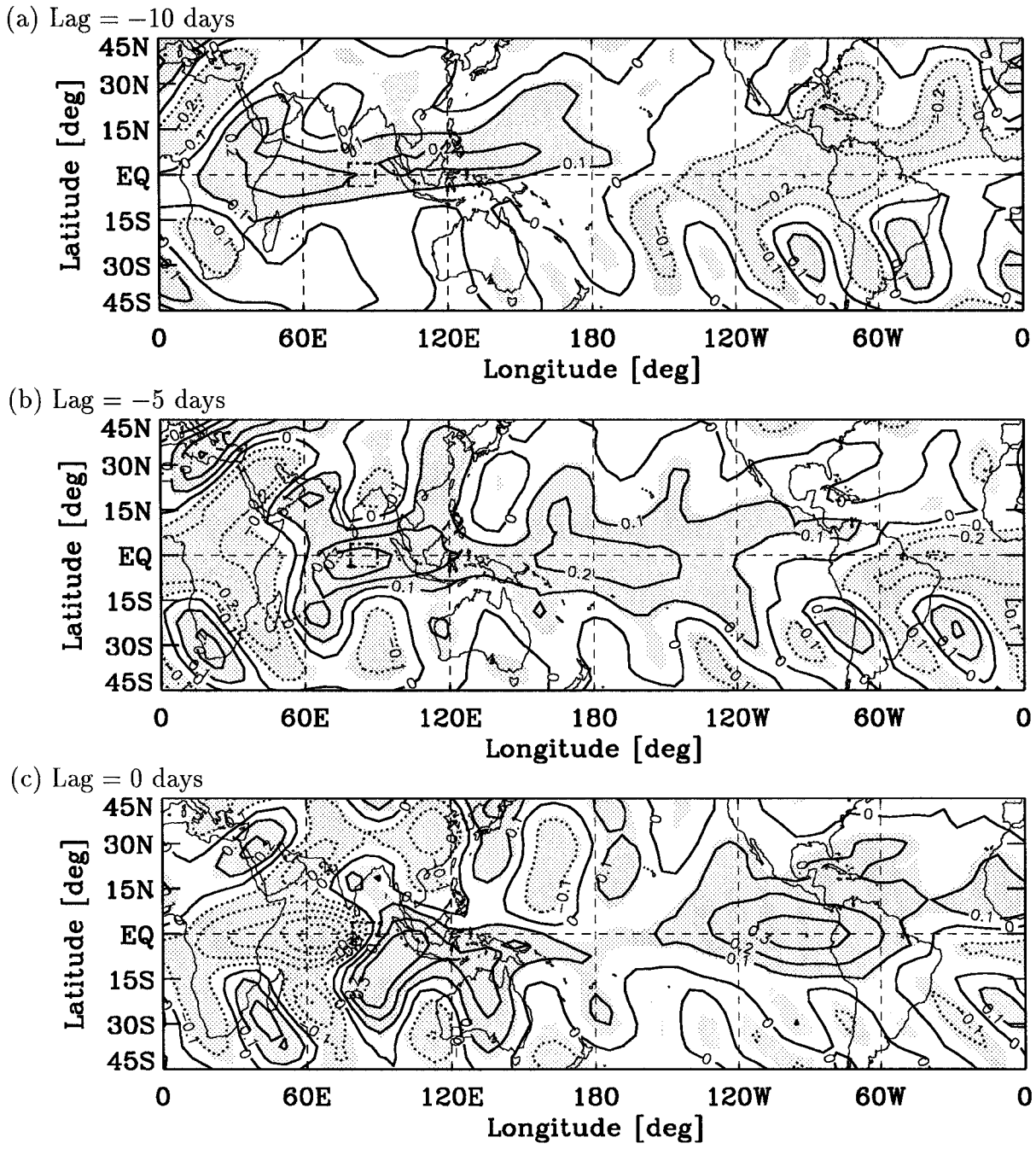

FIG. 8. Cross-correlation maps between OLR anomaly (spatial average of grid points in the region bounded by 78.75°–90°E and 3.75°S–3.75°N, as shown by the dashed-dot box), and 850-hPa zonal wind (u_{850}) anomaly (throughout the model domain). Lag correlation is formed between OLR(t) and $u_{850}(t + \text{lag})$. Positive (negative) correlations imply enhanced convection is associated with easterly (westerly) zonal wind anomalies. Correlations meeting the 95% confidence level are shaded. Contour interval is 0.1.

The operators $\langle\ \rangle = \widehat{(\ )} \equiv \Delta p_T^{-1} \int_{p_s}^{p_t} (\ )\, dp$ denote vertical averaging over the troposphere, from the surface (p_s) to the tropopause (p_t), where $p_T = p_s - p_t$. The variable η_a is a factor associated with the average of momentum equation, temperature equation, and moisture equation advection by baroclinic zonal mean wind, while η_d is a factor associated with the difference of advection in the momentum equation, with advection in the temperature and moisture equations. From the values given in NZ (Table 1), $\eta_a \approx 0.1$ and $\eta_d \approx 0.1$. The variables $\hat{a}_1$ and $\hat{b}_1$ are the vertical averages of the temperature and moisture basis functions, respectively, and κ (=0.286) is the ratio of the gas constant for air to the specific heat of air at constant pressure. Damping

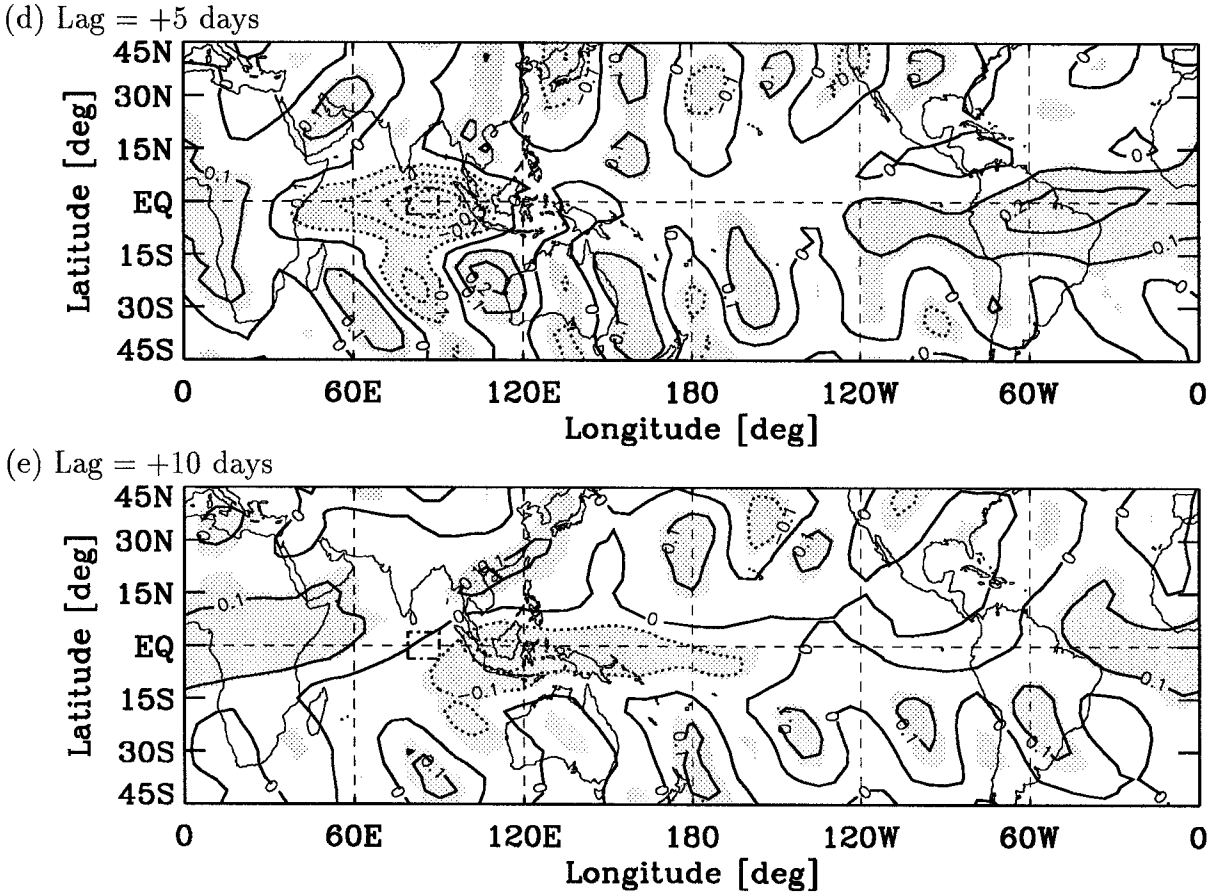

FIG. 8. (*Continued*)

effects would tend to decrease the phase speed. A typical value of the gross moist stability of the model in equatorial convective regions is 1.08×10^3 J kg^{-1} and is relatively constant with season. For these values, (1) suggests a phase speed of approximately 19 m s^{-1}, if advection were ignored, and roughly 4–18 m s^{-1} when advection is included. The variations in phase speed with the seasonal cycle in the model appear consistent with the effects of advection, as estimated from (1) as a function of season. The barotropic mean wind $\overline{u}_0$ provides the larger contribution, but the $\eta_a\overline{u}_1$ contribution of the baroclinic mean wind is also quite significant.

b. Spectral analysis

Figures 5 and 6 show the spectral analysis of the 250- and 850-hPa zonal wind anomalies and OLR anomalies for this control run. Slanted lines on the wavenumber–frequency plots in these figures represent phase velocity values of 5, 10, 20, and 30 m s^{-1}. The 850-hPa zonal wind spectra indicates that the intraseasonal signal is predominantly wavenumber 1 in structure, with a peak period of approximately 20–80 days (Figs. 5c and 5d). On the other hand, the 250-hPa zonal wind spectra shows peak power in the wavenumber-0 mode, with a period of about 160 days. OLR shows noticeable amounts of spectral power both at low and higher wavenumbers (3–7). In comparison to the zonal wind spectra, the OLR power is less concentrated. The peak at wavenumber 1 appears to be the highest, with a period of about 50 days. The wavenumber-0 peak has approximately the same period as the wavenumber-1 peak.

Following the method used by WK, Fig. 7 shows the OLR PSD presented in Fig. 6a, normalized by an estimate of background PSD. The background PSD is estimated by applying a 1–1–1 filter in frequency and wavenumber to the OLR PSD. The smoothing is applied 10 times to all frequencies; for frequencies above 0.125 day^{-1}, smoothing is applied an additional 50 times. In the similar figure in WK (their figure 3b), values above 1.1 are taken to indicate significance at the 95% level, assuming 500 degrees of freedom (DOF); these values are shaded. If similar assumptions were used for DOF, our spectra estimates would pass significance tests at a similar level, since our effective bandwidth is much smaller than that of WK's, but we use a much longer time series (45 yr vs approximately 18 yr in WK). Thus,

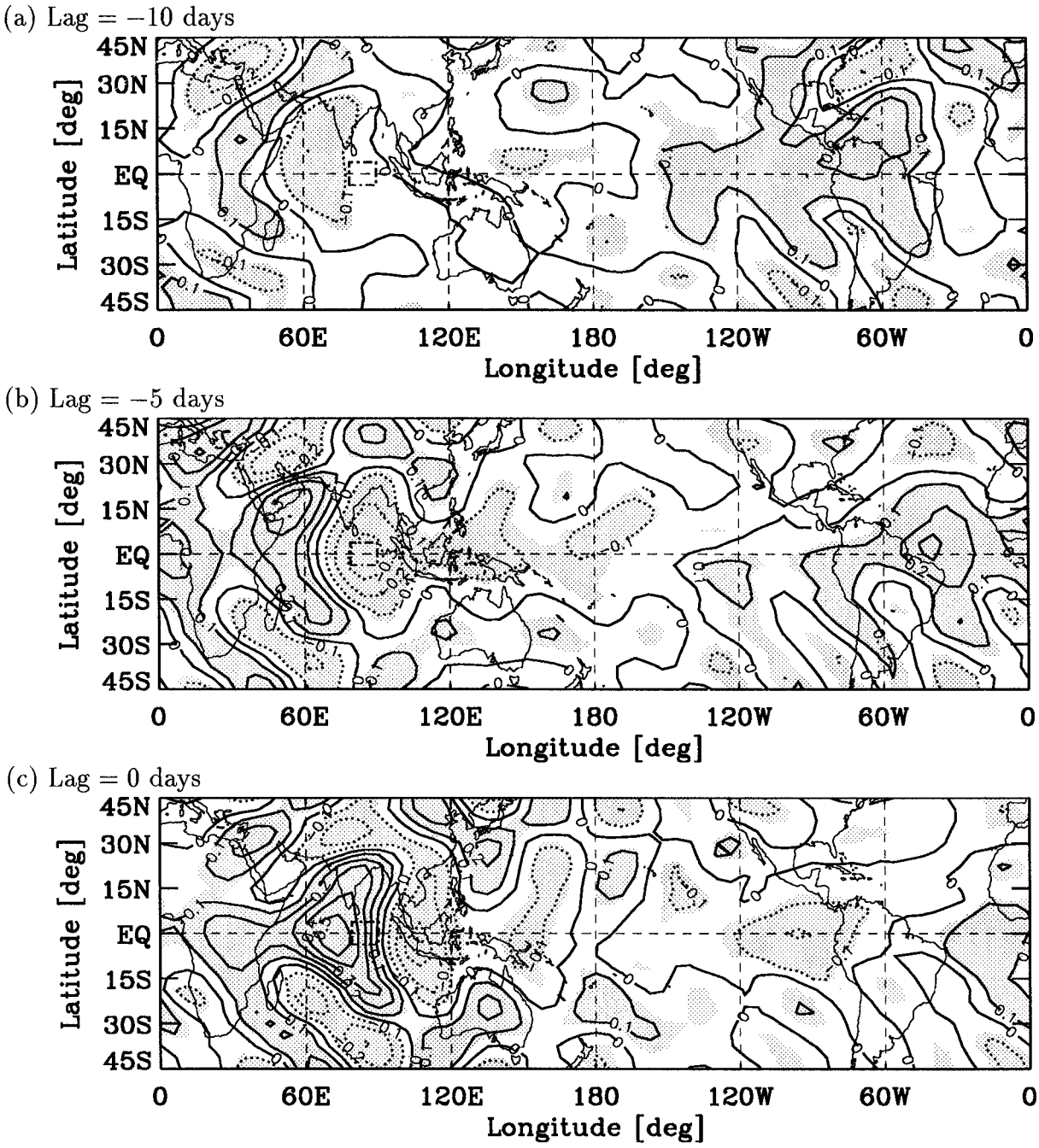

FIG. 9. As in Fig. 8, except cross-correlation maps between OLR anomaly (spatial average of grid points in the region shown by the dashed-dot box) and 250-hPa zonal wind (u_{250}) anomaly (throughout the model domain) are shown. Lag correlation is formed between OLR(t) and $u_{250}(t + \text{lag})$. Positive (negative) correlations imply that enhanced convection is associated with easterly (westerly) zonal wind anomalies. Contour interval is 0.1.

we also shade values above 1.1 in our Fig. 7 (although our contour interval differs from that used in WK's Fig. 3b). Other differences in our analysis methodology include the following: 1) our PSD is computed using OLR values averaged between 7.5°S and 7.5°N while their PSD is the sum of independently calculated OLR PSD computed for each latitude band between 15°S and 15°N from a 2.5° gridded dataset; 2) our background spectrum is computed slightly differently, in terms of both the filter used (1–1–1) and the number of passes it is applied.

WK's Fig. 3b shows an enhancement of spectral power in OLR in a curve with dispersion characteristics similar to those predicted by linear equatorial Kelvin wave theory but with phase speeds consistent with a

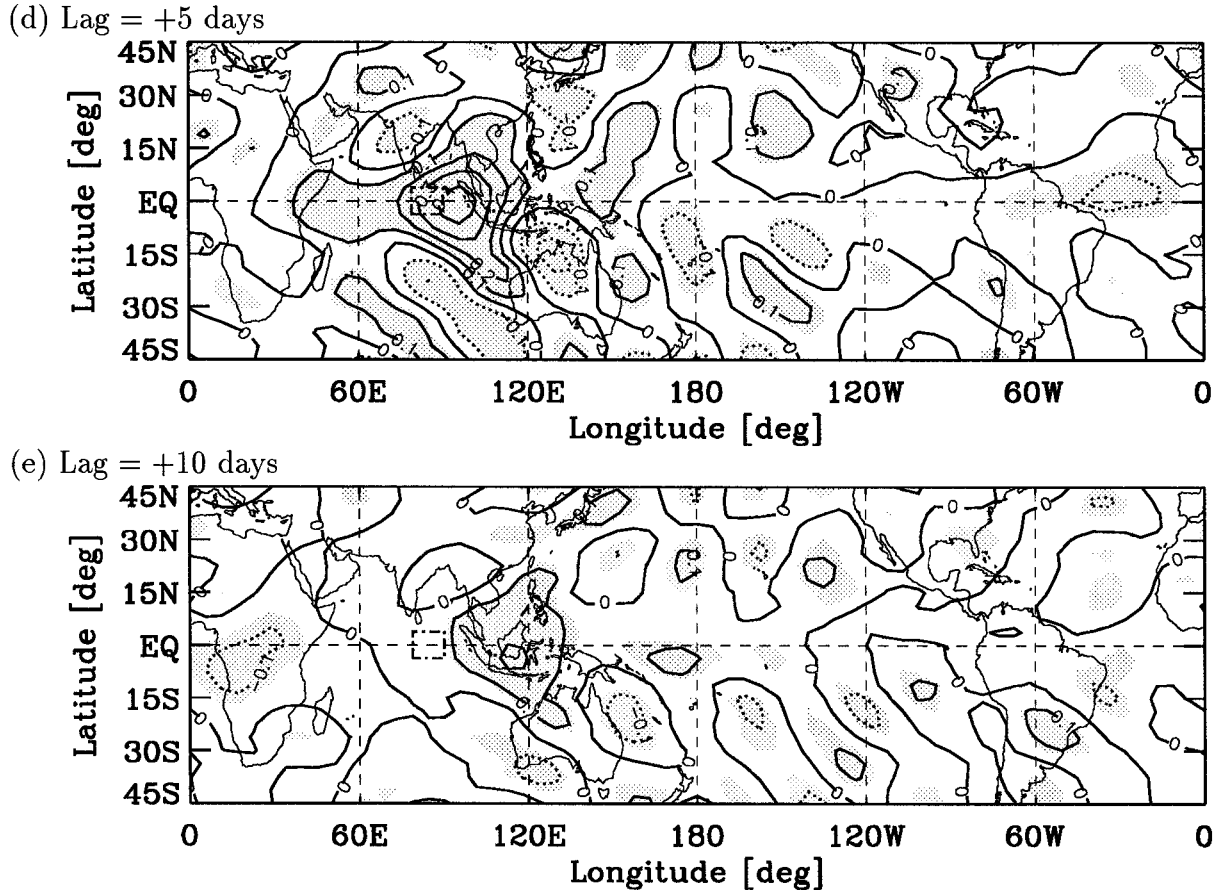

FIG. 9. (*Continued*)

moist Kelvin wave. As frequency and wavenumber increase, the apparent phase speed for the maximum of the spectral enhancement slows from approximately 22 m s^{-1} at wavenumber 2 to 16 m s^{-1} at wavenumber 6, although a considerable spread is found at each wavenumber. At wavenumber 1, this moist Kelvin wave overlaps with the region WK have associated with the MJO. At other wavenumbers, WK's MJO mode shows dispersion characteristics quite unlike those predicted by linear equatorial wave theory. In particular, this MJO signal shows significant spectral power at a broad range of eastward zonal wavelengths, at a near-constant period (about 30–60 days).

The OLR signal produced by the QTCM1 (Fig. 7) shows similar features. The moist Kelvin wave simulated by QTCM1 is only slightly less dispersive than that seen in WK, although the QTCM1 simulation does split in wavenumber, something not seen in WK's analysis. The wavenumber-1 Kelvin wave PSD is extended to higher wavenumbers at the same period, similar to the behavior shown by WK for the MJO band. This simulated MJO band extends to higher wavenumbers than WK's. Nonetheless, the model appears to have qualitative counterparts to the features noted by WK, including the distinction, as frequency and wavenumber increase, between moist Kelvin waves and the extension of MJO variability into higher wavenumbers.

c. Lag-correlation structure

Lag-correlation plots for OLR anomaly (in the region bounded by 78.75°–90°E and 3.75°S–3.75°N) versus lower- and upper-level zonal wind anomaly and evaporation anomaly (throughout the model domain) are given in Figs. 8, 9, and 10, respectively. The domain of the OLR reference time series (hereafter ''reference region'') is chosen to match Salby and Hendon's (1994) finding that the largest convection signal is located on the equator at 84°E. For the QTCM1 simulation, spectral analysis of the spatial mean (nonareally weighted) in this reference region shows peak power at a period of approximately 15–25 days (not shown). This lag-correlation analysis is similar to the lag-regression analysis of Hendon and Salby (1994). However, Hendon and Salby bandpass-filter their data to retain eastward periods of 35–95 days and spatially filter their data to retain wavenumbers 1–3, whereas the lag correlations shown in this current study do not. Because negative

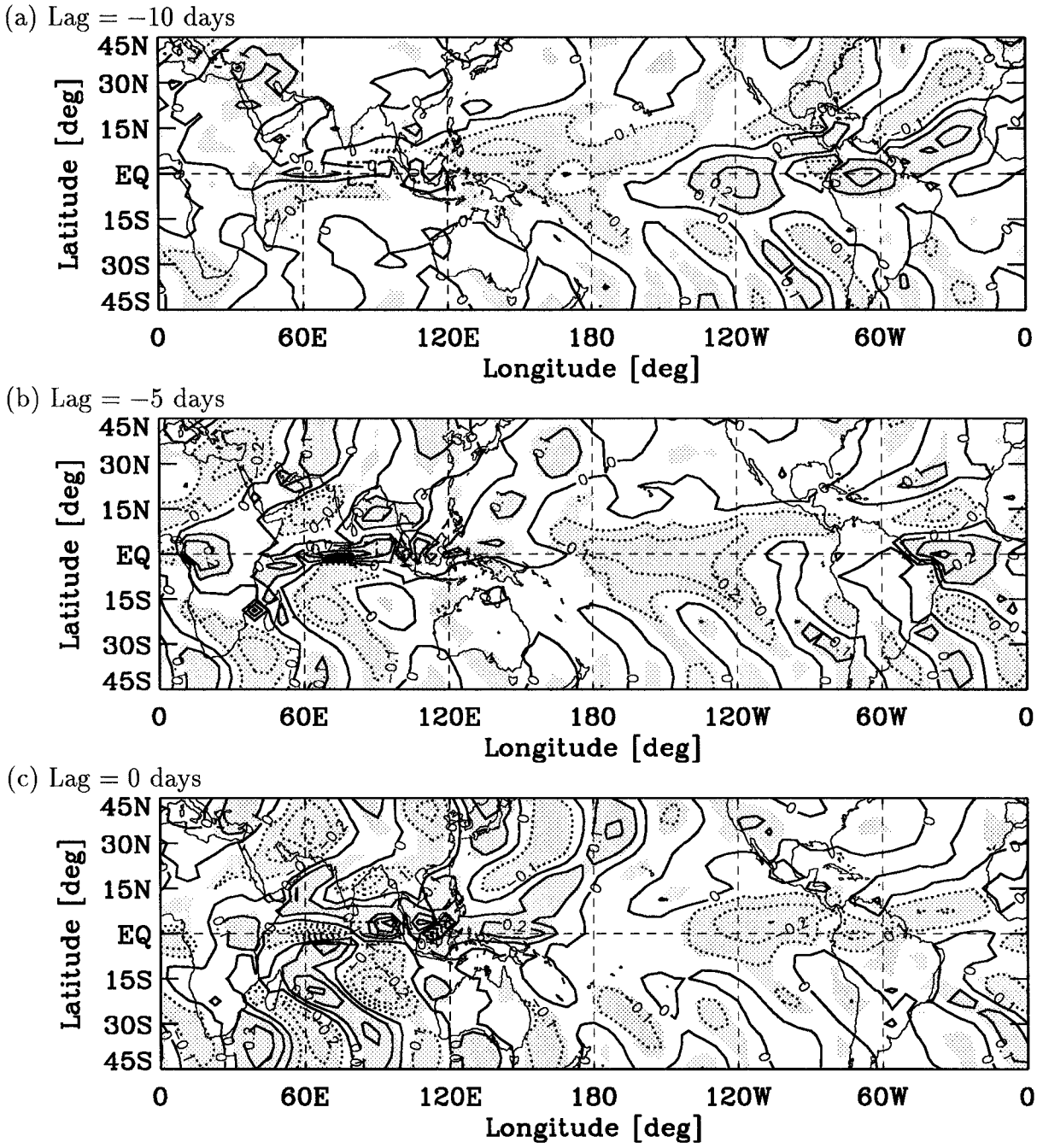

FIG. 10. As in Fig. 8, except cross-correlation maps between OLR anomaly (spatial average of grid points in the region shown by the dashed-dot box) and evaporation anomaly (throughout the model domain) are shown. Lag correlation is formed between OLR(t) and evaporation(t + lag). Positive (negative) correlations imply enhanced convection is associated with negative (positive) evaporation anomalies. Contour interval is 0.1.

OLR anomalies imply enhanced convection, positive correlations between OLR and zonal wind imply that enhanced convection is associated with negative (i.e., easterly) zonal wind anomalies, while negative correlations imply that enhanced convection is associated with positive (i.e., westerly) zonal wind anomalies. Positive correlations between OLR and evaporation anomaly imply that enhanced convection is associated with suppressed evaporation, while negative correlations imply that enhanced convection is associated with enhanced evaporation.

Cross correlations significantly different from zero at the 95% confidence level are shaded. Significance is calculated using a one-sided Student's t-test (Brooks and

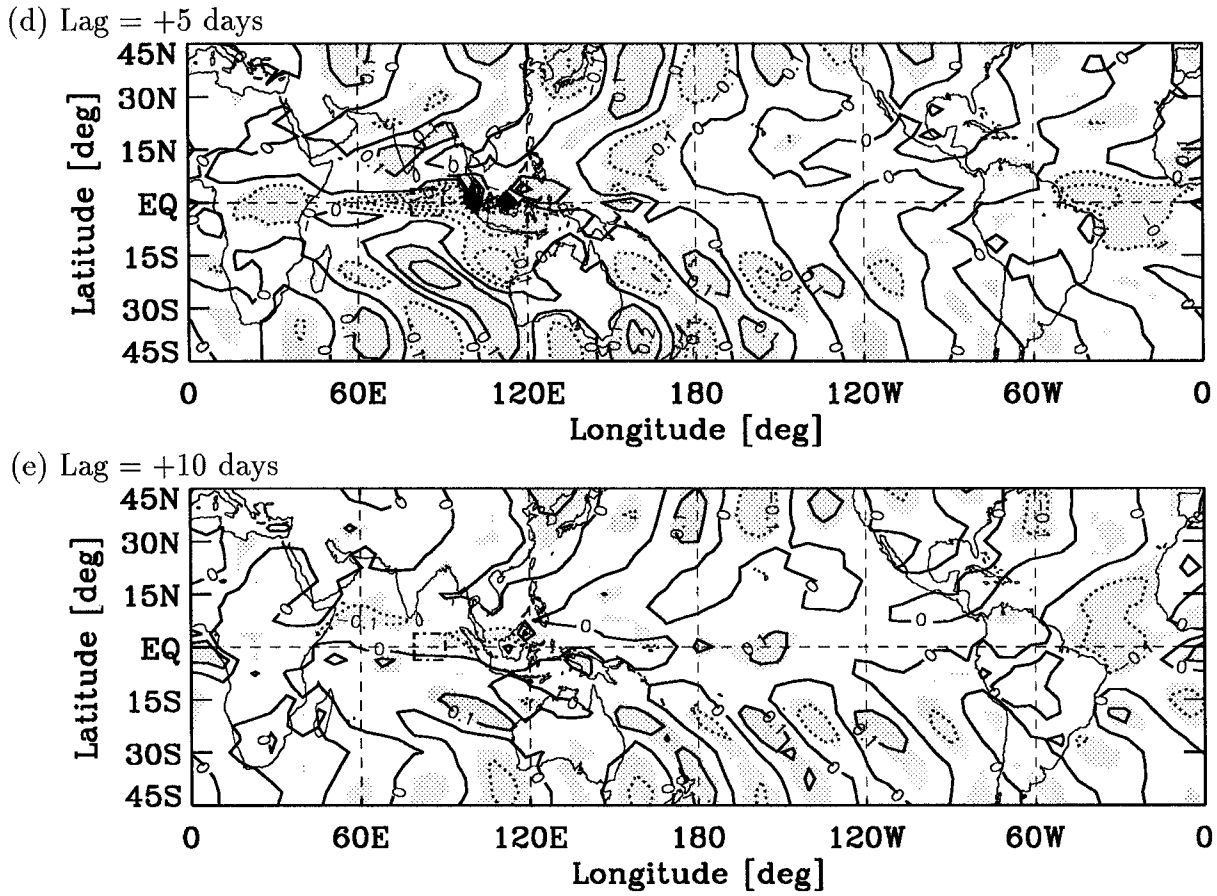

FIG. 10. (*Continued*)

Carruthers 1953, p. 220) and an effective degree of freedom (EDOF) given by EDOF $= N\Delta t/\tau$, where N is the number of Δt output time intervals and τ is an estimate of the ''effective time between independent samples,'' based upon autocorrelations of each of the cross-correlated fields (Livezey and Chen 1983). For all cross-correlation plots, $N = 1800$ and $\Delta t = 1$ day. These correlation maps utilize anomalies that are calculated by removing daily deviations from a spline fit to the monthly climatology over a 5-yr analysis period versus a 45-yr period as in the case of the time–longitude and spectral density plots. Depending on the case, τ varies from a maximum of 3.4–2.8 days to a minimum of about 2.1 days. Thus, EDOF varies from a minimum of approximately 530–640 to a maximum of about 850–870. In addition, the patterns for the lag-correlation plots discussed (i.e., lags from -15 to $+15$ days) all meet the 95% pattern confidence level, assuming spatial independence (see Livezey and Chen 1983).

The lag-correlation maps for OLR versus 850-hPa zonal wind (Fig. 8) show an equatorial wavenumber-1 feature extending throughout the lags shown (as well as lag $= -15$ days, which is not shown). At lag $= -10$ days, the easterly zonal wind anomaly phase of the equatorial wave spans the Indian and western Pacific Oceans while the westerly phase lies over the eastern Pacific and Atlantic Oceans. Over time, this wavenumber-1 feature propagates eastward. At lag $= 0$ days (Fig. 8c), the feature is positioned so that there is lower-level zonal wind convergence into the region of enhanced convection, with easterly winds to the east of the OLR reference region and westerly winds to the west of the reference region. The pattern continues to propagate eastward until lag $= +10$ days (Fig. 8e), when the westerly zonal wind anomaly phase is centered over New Guinea. By lag $= +15$ days (not shown), the wavenumber-1 signal is no longer observed.

Besides being eastward propagating, this wavenumber-1 feature also shows atmospheric moist Kelvin wave structure; it is zonally elongated with a meridional extent on the order of the Rossby deformation radius. However, the pattern of the feature is more complicated than a moist Kelvin wave. In particular, there appear to be correlations with extratropical features that have scales on the order of the midlatitude deformation radius. If the pattern was decomposed into meridional structures associated with equatorial waves, there would be Rossby wave components coupled to the moist

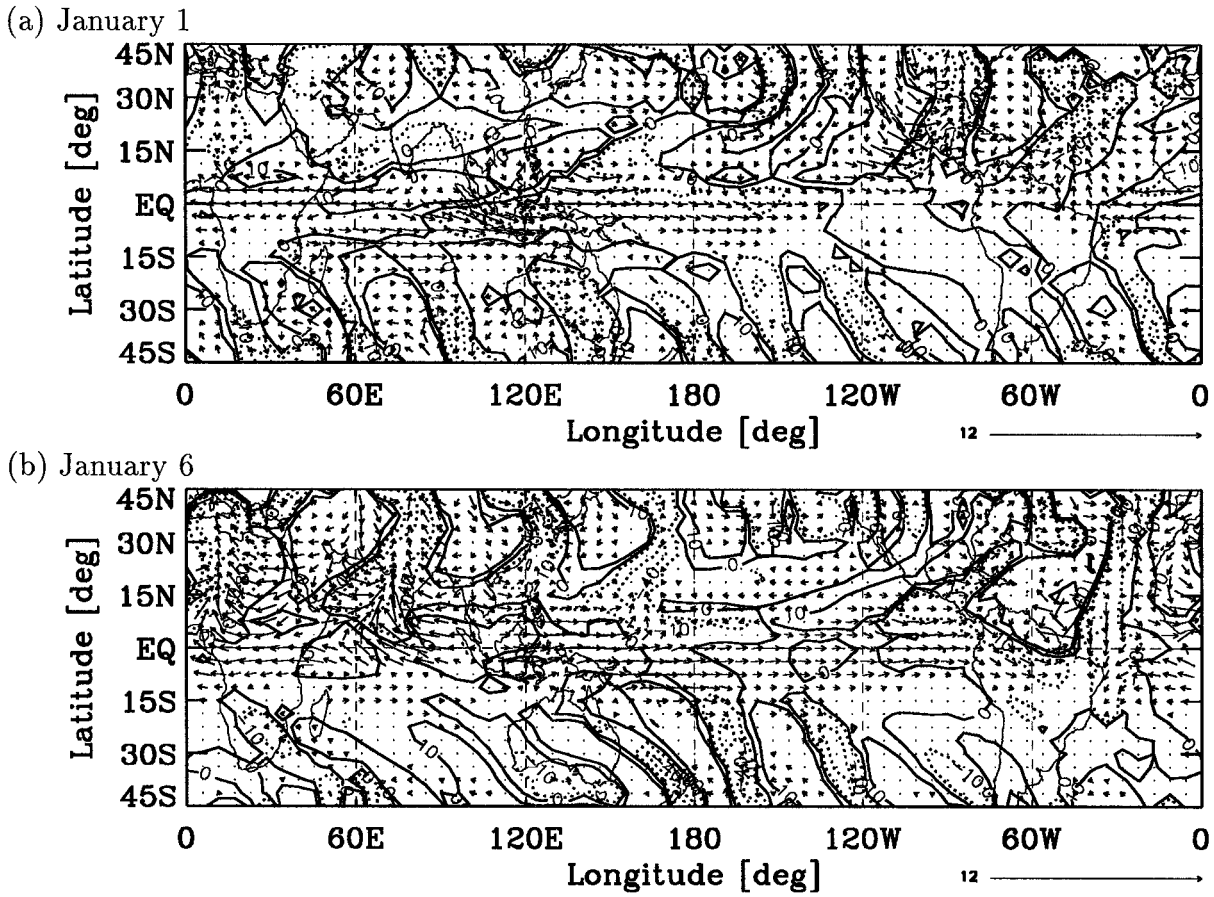

FIG. 11. Examples from the analysis year 1 Jan moist-Kelvin/MJO-like event (analysis year 1 is year 2 of the run; year 1 of the run was discarded as spinup). OLR (contours) and 850-hPa wind (vectors) anomalies are shown for (a) day 1 (1 Jan) and (b) day 6 (6 Jan). The time–longitude counterparts for the OLR and 850-hPa zonal wind are Figs. 4 and 3b, respectively. Negative OLR anomalies are dotted. The wind is displayed using a magnitude scaling that is a function of latitude, as described by (2). The scaling vector given in the lower right-hand corner is in m s^{-1} and applies to winds at the equator. Wind arrows are centered at each grid point. Arrows less than approximately 1/5 of a grid box in length are shown as dots. OLR contours are plotted at −80, −40, −10, 0, 10, and 40 W m^{-2}.

Kelvin wave. The phasing of wind and OLR anomalies appears to be more like a moist Kelvin wave than similar figures in Hendon and Salby (1994), but their data were filtered to low wavenumbers and frequencies while Figs. 8 and 9 are not.

Like the OLR–850-hPa zonal wind cross correlations (Fig. 8), the OLR–250-hPa zonal wind cross correlations (Fig. 9) show an equatorial eastward-propagating wavenumber-1 feature. However, the OLR–250-hPa zonal wind cross correlations (Fig. 9) are not mirrored reproductions of the lower-level correlations but instead exhibit noticeably different behavior. First, the clear wavenumber-1 pattern that is observed in the OLR–850-hPa zonal wind correlations (Fig. 8) tends to be broken up in the 250-hPa case by additional patterns. The spatial extents of the eastward and westward phases of the upper-level maps are not as coherent, a feature most clearly seen when comparing the correlation maps at lag = −10 days (Figs. 9a and 8a) and lag = −5 days (Figs. 9b and 8b). However, here too, as in the lower-level case, there are significant correlations between the OLR reference zone and zonal winds in the midlatitudes.

Lag-correlation maps are also plotted for the OLR anomaly versus the evaporation anomaly (Fig. 10). As with the OLR–zonal wind correlation maps, the evaporation correlation maps show evidence of a wavenumber 1, eastward-propagating feature. However, the evaporation response to convective heating in the OLR reference region is more complicated than the simplest EWF formulation would suggest. First, while the evaporation response is zonally elongated, the extratropics also show statistically significant evaporation responses, presumably the evaporation signature of other midlatitude correlations. However, while the evaporation correlation patterns qualitatively resemble the lower-level wind anomaly patterns, taking into account the spatial variation in climatological winds (easterlies over the Pacific, weak winds in the Indonesian region, and westerlies over the Indian Ocean), and while the lower-level winds behave generally like a Kelvin wave,

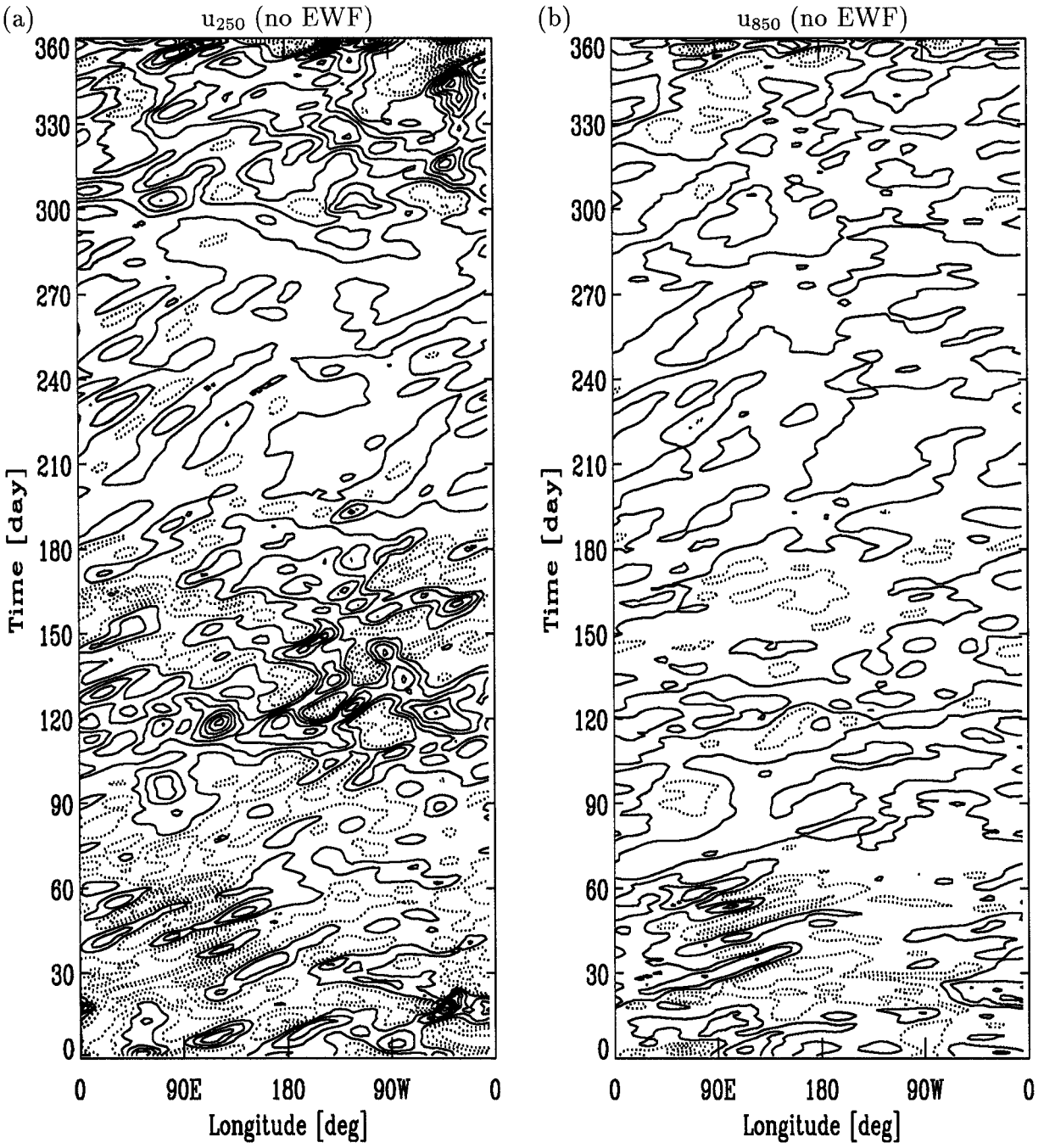

FIG. 12. As in Fig. 3, except the EWF is removed. Zonal wind anomaly is shown at (a) 250 hPa (contour 1 m s^{-1}) and (b) 850 hPa (contour 0.5 m s^{-1}).

the evaporation pattern is not entirely what one would expect based on the simplest EWF theory. For instance, at lag = −10 days (Fig. 10a), enhanced convection is associated with enhanced equatorial evaporation immediately east of the OLR reference region and suppressed equatorial evaporation immediately west of the reference region. However, at lag = −5 days (Fig. 10b), enhanced convection is associated with suppressed evaporation both immediately east *and* west of the reference region. And at lag = 0 days and lag = +5 days (Figs. 10c and 10d), the correlation signs tend to be *opposite* those at lag = −10 days, with enhanced convection in the OLR reference region being associated with suppressed evaporation to the east and enhanced evaporation to the west (as has been seen in observations).

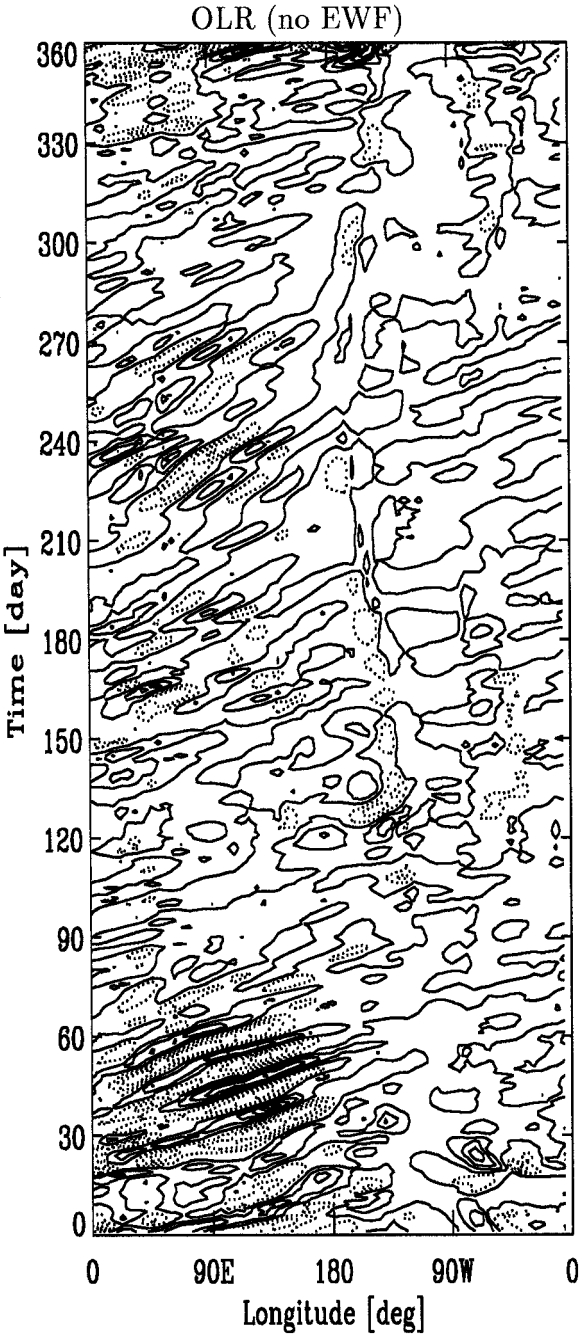

FIG. 13. As in Fig. 4, except OLR anomaly (contour 5 W m^{-2}) is shown for the EWF removed.

d. Examples of synoptic structure

To help paint a rough picture of the interaction between the extratropics and Tropics in this model, plots for days 1 (1 January) and 6 (6 January) of the first year of the 45-yr analysis period are given in Figs. 11a and 11b, respectively. OLR and 850-hPa wind anomalies (deviations from the 45-yr climatology) are shown. These plots serve as examples of particular days in a moist-Kelvin/MJO-like event corresponding to the extended eastward-propagating intraseasonal signal seen during most of January (days 0–30) in the time–longitude plots for OLR and 850-hPa zonal wind (Figs. 3b and 4). Because tropical wind anomalies are much weaker than their extratropical counterparts, the lengths of the wind vectors shown in Fig. 11 are scaled by a factor $\mathcal{F}(\phi)$, which is Gaussian in latitude ϕ:

$$\mathcal{F}(\phi) = \frac{A}{\sigma\sqrt{2\pi}} e^{-(1/2)\phi^2/\sigma^2} + B, \qquad (2)$$

where $\sigma = 10$ deg, $A = 250$, and $B = 1$. This scaling factor accentuates vector lengths for latitudes between approximately 30°S and 30°N, with a maximum factor (of about 11) applied to winds at the equator, falling off to a minimum factor of about 1 for latitudes beyond 30°S and 30°N.

Extratropical disturbances in this model tend to have a preferred wavenumber, on the order of wavenumber 8, and are centered at around 30°N and 30°S. Intermittently, tails from these storms reach down into the Tropics. The simulated storms have a qualitatively realistic seasonal dependence, with stronger disturbances in the Southern Hemisphere during southern winter and stronger Northern Hemispheric storms during northern winter. However, these simulated midlatitude disturbances are more regular than observed, often moving as a coherent wave packet of several successive storms, as they propagate eastward around the globe. In addition, the model's midlatitude disturbances have more intense precipitation than observed, although the zonal wind variance is roughly half that of the observed. In the time slices shown, negative OLR anomalies correspond to heightened storm activity.

Figure 11a shows a situation with reasonably little interaction between the Tropics and extratropics over the sector 0°–120°E. Tropical wind anomalies are predominantly zonal and low wavenumber, as consistent with the MJO. Over most of the domain, winds generated by midlatitude storms do not show pronounced entry into the Tropics. Likewise, the OLR anomalies associated with the extratropical disturbances remain mostly outside of the Tropics. In contrast, on day 6 (Fig. 11b), the winds associated with the extratropical disturbances intrude noticeably into the Tropics, and OLR anomalies also extend down into the Tropics; however, while these extratropical disturbances vary on a fairly short timescale, the tropical anomalies appear to vary more slowly. In both Figs. 11a and 11b, the equatorial winds retain a global structure, with easterlies extending westward from the Pacific warm pool to South America and westerlies east of the warm pool to South America. Even when extratropical influence is occurring, one can distinguish the moist-Kelvin/MJO-like pattern and eastward propagation of this global structure.

Figures 11a and 11b illustrate that the interaction between the extratropics and Tropics is complicated, with

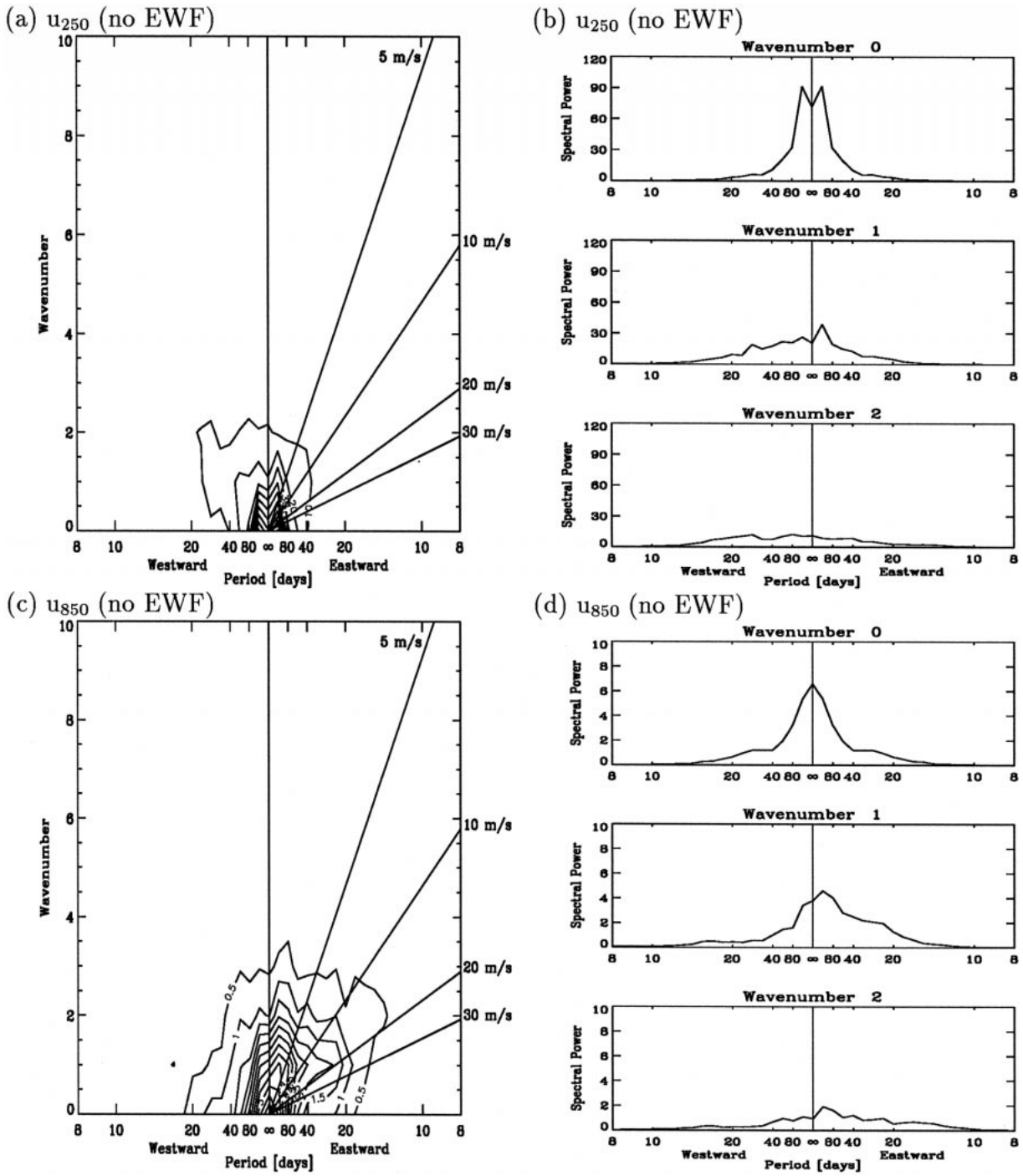

FIG. 14. As in Fig. 5, except the EWF is removed. PSD as wavenumber–frequency contour plots and wavenumber 0–2 slices are shown. (a) and (b) show 250-hPa zonal wind, and (c) and (d) show 850-hPa zonal wind. Units of $(\text{m s}^{-1})^2$. Contour intervals are (a) 10 and (c) 0.5. Standard deviation of PSDs is 10%.

no readily apparent simple explanation. Other time slices (not shown) tell a similar story, where extratropical interaction with the Tropics is aperiodic and intermittent and where the Tropics and extratropical disturbances evolve on different timescales and spatial scales.

e. Summary of control run features

In several aspects, the QTCM1 simulated moist-Kelvin/MJO-like oscillation reproduces features found in the observed intraseasonal oscillation. First, the mod-

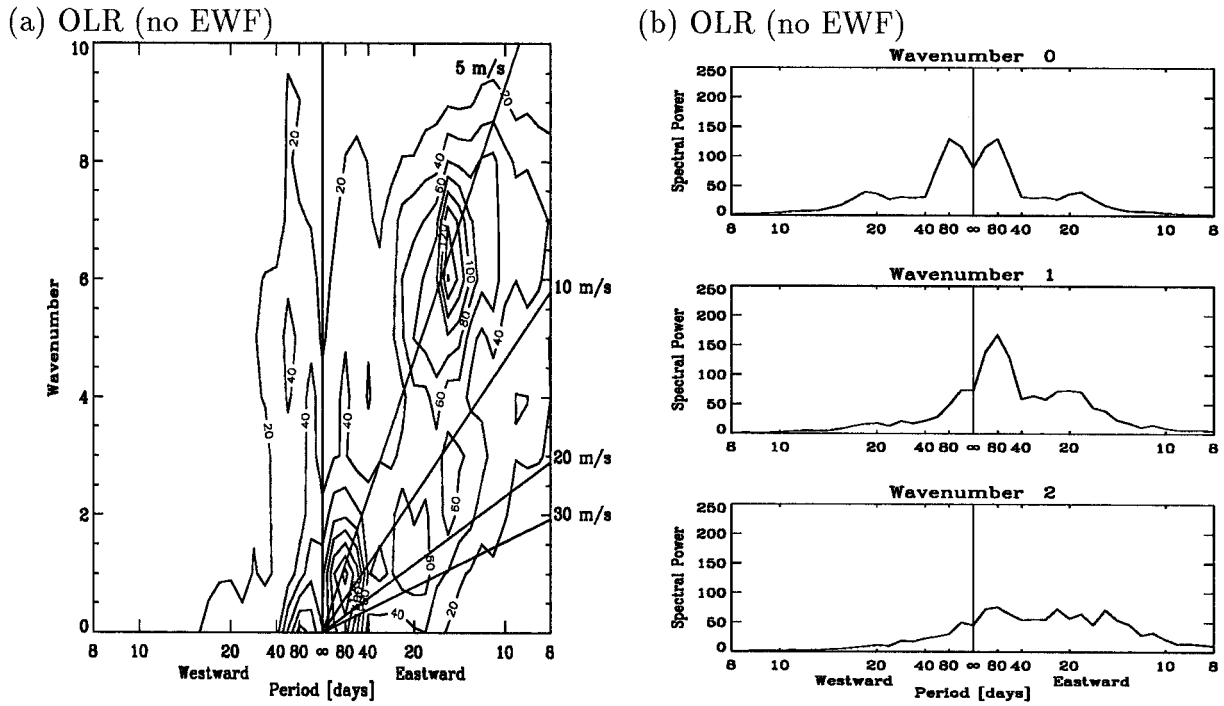

FIG. 15. As in Fig. 6, except PSD for the EWF removed is shown. Units of $(W\ m^{-2})^2$. Contour interval for (a) is 20. Standard deviation of PSDs is 10%.

el oscillation exhibits a variable phase speed, both temporally and spatially. In addition, the propagating convective feature simulated by the model is confined to the Eastern Hemisphere. Upper- and lower-level zonal wind anomalies, while exhibiting different behavior, are approximately out of phase with each other. Lower-level zonal wind anomalies show cases of phase speed changing with longitude, with lower phase speeds in the Indian Ocean and western Pacific and higher phase speeds in the central and eastern Pacific. Seasonality of the amplitude of the oscillation, as measured by upper-level zonal wind variance, also shows similarity to observations (Madden and Julian 1994). Frequency-wavenumber analysis of OLR spectra shows moist Kelvin and MJO structure similar to that found in observations (WK). In particular, QTCM1-simulated OLR also shows levels of spectral power significantly greater than background power at several wavenumbers in the MJO frequency band. In section 5, a preliminary hypothesis is presented to explain this feature of the MJO.

However, while the phase speed and period of the model-simulated intraseasonal oscillation are generally reasonable, the phase speed of the zonal wind (particularly lower-level zonal wind) appears too fast. In the upper-level zonal winds, there is apparently a great deal of variance associated with non-MJO timescale phenomena, which yields larger variance than expected at low frequency and wavenumber 0. The magnitude of this (the extra variance at upper levels) actually makes the moist-Kelvin/MJO-like signal easier to diagnose in the lower-level winds, unlike observations where the upper-level signal is often clearer. Finally, the magnitude of the anomalies is generally lower than that given in observational studies (e.g., Knutson and Weickmann 1987; Hsu et al. 1990). All in all, considering that the model includes only two vertical wind structures, it is interesting that the simulated intraseasonal variability is so complex.

The OLR–zonal wind and OLR–evaporation lag-correlation maps also show an oscillation with features similar to the observed MJO: equatorial, eastward-propagating, zonally elongated, and predominantly wavenumber 1. The structure of these lag-correlation maps also suggest possible insights into the tropical dynamics and behavior of moist Kelvin waves and/or the MJO. First, for both of the OLR–zonal wind lag-correlation maps as well as the OLR-evaporation maps, there is a greater area of statistically significant correlations at negative lags as compared to positive lags. This suggests the zonal circulation and evaporation influences future convection more than convection influences the zonal circulation and evaporation, although not conclusively so. Second, we speculate that the differences between the OLR lag correlations with lower- and upper-level zonal wind might be due to the reduction in easterlies aloft. This would enable midlatitude Rossby wave variance to more easily penetrate equatorward at upper levels. Finally, the presence of

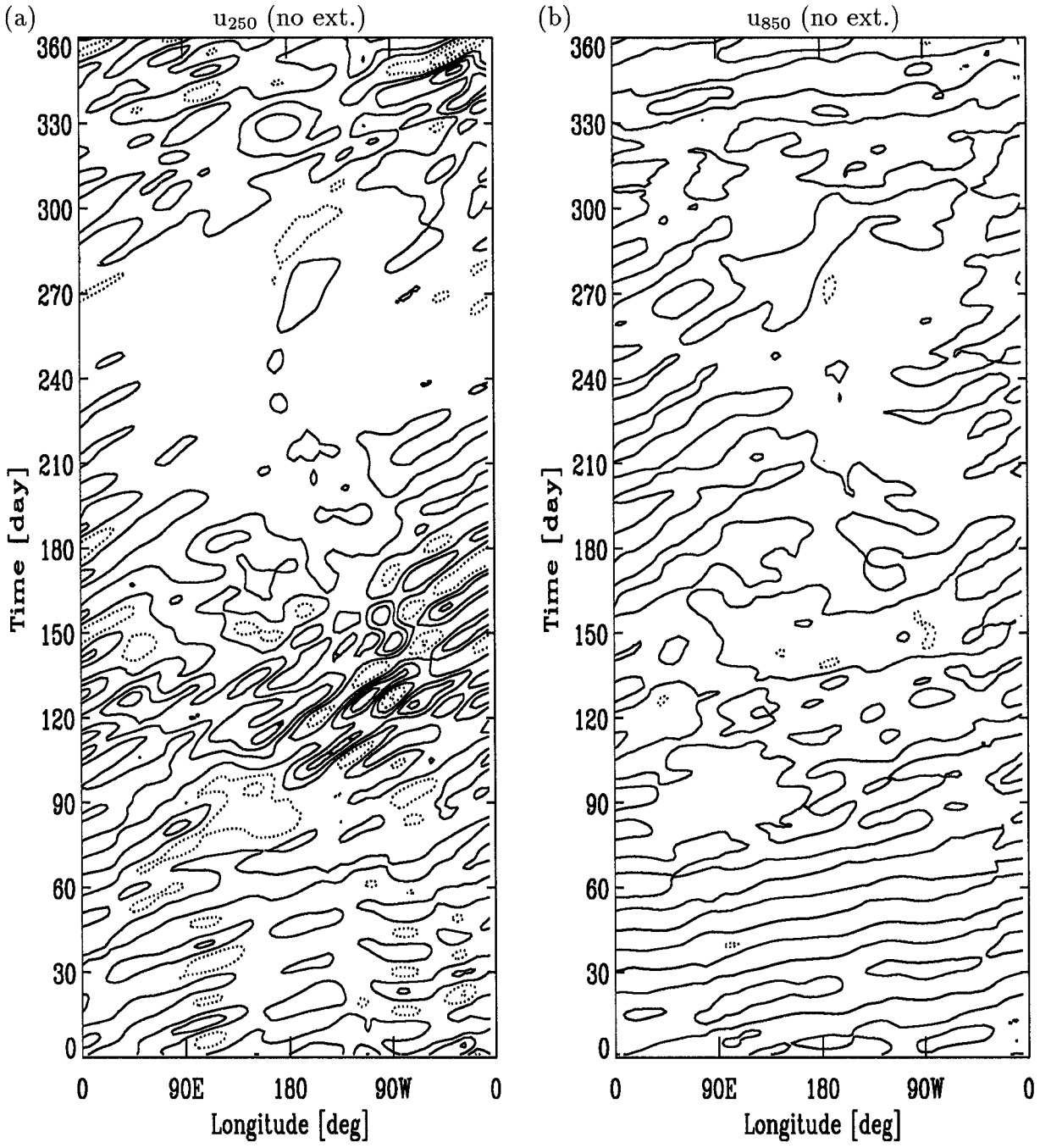

FIG. 16. As in Fig. 3, except extratropical excitation is removed. Zonal wind anomaly is shown at (a) 250 hPa (contour 1 m s^{-1}) and (b) 850 hPa (contour 0.5 m s^{-1}).

statistically significant correlations between the tropical OLR reference region and extratropical zonal wind (particularly for negative and contemporaneous lags) suggests that the extratropics may play a role in maintaining the model intraseasonal oscillation. The presence of OLR–evaporation correlations raises the question of what role the EWF may play in maintaining intraseasonal variance. However, the relationship appears so complex that it is not obvious what the precise EWF role is (i.e., maintaining, damping, or modifying). Fortunately, modeling experiments can help determine the EWF role. Such numerical experiments, investigating the effects of the evaporation–wind feedback and extratropical excitation on the QTCM1 simulated intraseasonal oscillation, are examined in sections 4a and 4b, respectively.

4. Model tests of proposed intraseasonal oscillation maintenance mechanisms

This study examines two specific proposed maintenance mechanisms for intraseasonal variability: evaporation–wind feedback (EWF) and extratropical excitation. Evaporation is commonly parameterized by a bulk-aerodynamic formula. QTCM1 also uses such a parameterization (NZ) given by

$$E = \rho_{\text{air}} c_p C_D V_s (q_{\text{sat}} - q_{\text{rs}} - b_{1\text{s}} q_1), \tag{3}$$

where ρ_{air} is the density of air, c_p is the specific heat at constant pressure, and C_D is the drag coefficient. Variables q_{sat}, q_{rs}, q_1 are the saturation humidity, a ''reference profile'' humidity, and the baroclinic mode moisture, respectively, all at the surface. Parameter $b_{1\text{s}}$ is the surface value of the Galerkin expansion coefficient for the baroclinic-mode moisture. For a further description of the reference profiles as well as the Galerkin expansion coefficients, see NZ. The surface wind speed V_s is parameterized in this model version for the purposes of calculating evaporation as $\sqrt{u^2 + v^2}$ at 900 hPa, bounded by a minimum (4 m s^{-1}) and a maximum (8 m s^{-1}) value. The minimum evaporation wind speed is provided to simulate the evaporation that exists in a grid box even when the winds calculated at the grid points are zero. This differs slightly from the revised model version of ZNC.

In the EWF scenario (Emanuel 1987; Neelin et al. 1987), surface wind anomalies induced by atmospheric heating create anomalous evaporation, which, if in suitable phase with the disturbance, enhance the convection, assisting in maintenance of the disturbance. To remove the effect of the EWF, V_s in (3) is replaced with a value constant in time (though still varying in space). In the tests described in section 4a, evaporation is calculated with mean wind magnitudes computed from a three-year QTCM1 run forced by seasonal SSTs. This analysis of the effects of the EWF does not account for seasonal changes in wind.

In this study, we use what we believe is a new technique to remove the effects of extratropical disturbances by replacing the effects of temperature advection with its annual mean value. This suppresses baroclinic instability, since perturbation advection of mean temperature gradients provides the energy source for such instability. The temperature equation solved by QTCM1 is the temperature associated with the first baroclinic mode (T_1) and is given by (NZ)

$$\hat{a}_1(\partial_t + \mathcal{D}_{T1})T_1 + M_{S1}\nabla \cdot \mathbf{v}_1 = \epsilon_c^*(q_1 - T_1) + F^{\text{RSH}},$$

where a_1 is the Galerkin expansion coefficient for the baroclinic mode for temperature, ϵ_c^* is inversely proportional to the convective timescale τ_c, $\mathbf{v}_1$ is the horizontal velocity vector, M_{S1} is the contribution of the dry stability to the gross moist stability, and F^{RSH} includes longwave radiation flux components, sensible heat flux at the surface, and shortwave fluxes at the surface and top of atmosphere. Again, the operator $\widehat{(\,)}$ denotes vertical averaging over the troposphere. The variable $\mathcal{D}_{T1}$ includes the horizontal advection-related terms. These horizontal advection terms will be referred to as advT1 in this paper. Since

$$T_1 = \frac{\int_{p_s}^{p_t} T \cdot a_1(p)\, dp}{\int_{p_s}^{p_t} a_1(p)\, dp}.$$

Then, advection projected onto T_1 (advT1) is

$$\text{advT1} = -\frac{\int_{p_s}^{p_t} \mathbf{v}(p) \cdot \nabla T(p) a_1(p)\, dp}{\int_{p_s}^{p_t} a_1(p)\, dp}.$$

To remove the effects of baroclinic temperature advection, advT1 is not allowed to vary in time but instead is set to its three-year mean value from a control run, that is, advT1 $\equiv$ $(\overline{\text{advT1}})_{\text{control}}$. This is done to retain the average effect of transient eddy heat transport so the climatology does not change dramatically. As in the case with turning off the EWF, the effects of seasonal changes in advT1 are not accounted for. The direct effects of the $\mathbf{v} \cdot \nabla T$ terms tend to be small in the Tropics, and indeed most non-GCM models of the Tropics neglect these terms.

The following cases are simulated: 1) a control run, using the standard version of QTCM1 v1.0, with evaporation–wind feedback and extratropical disturbances included; 2) evaporation–wind feedback turned off; 3) extratropical disturbances turned off; and 4) both the EWF and extratropical disturbances turned off. Among all the above cases, a comparison of monthly mean values for January and July indicated no great difference in the simulated climatology (not shown). However, for cases 2 and 4, the magnitude and extent of the Southern Pacific Convergence Zone (SPCZ) increased noticeably during January.

a. Effect of evaporation–wind feedback

When the EWF is turned off, equatorial anomaly intensities in upper- and lower-level zonal wind and OLR generally decrease. Figure 12 shows the time–longitude plot for upper-level and lower-level zonal wind anomaly for the case of the EWF removed (EWF off). Figure 13 shows the OLR anomaly for the EWF-off case. Overall, zonal wind and OLR anomalies weaken at all longitudes. This is most noticeable for June–August (JJA) and September–November (SON). However, one interesting local effect is that February OLR anomalies in the western Pacific intensify.

When the EWF is removed, the phase speed of OLR

anomalies (Fig. 13) drops slightly. This effect is more pronounced during JJA and SON than December–February (DJF). This appears to be true both east and west of the date line. The removal of the EWF also appears to degrade the coherency of phase speed in certain regions during these months. In particular, it is harder to identify a propagating signal east of the date line. For the zonal wind anomalies (Fig. 12), the removal of the EWF does not seem to change phase speed much for either 250- or 850-hPa winds (for times when phase speeds can be identified). An apparent emphasis on lower-frequency oscillations may be noted, sometimes with eastward propagation.

In spectral power (Fig. 14), removing the EWF has selected effects on the frequency distribution of power. For upper-level zonal wind, power in the 20–40-day band drops to approximately half of its control run value (Fig. 5). There is also a 50% decrease in *westward* power for periods greater than about 100 days. In lower-level zonal wind, the 20–40-day spectral peaks in the wavenumber-1 component decrease by more than 50% when the EWF is removed; at the same time, an eastward-propagating peak with a period of about 160 days emerges, with a magnitude approximately one-third higher than in the EWF case (Figs. 14c and 14d).

For OLR, turning off the EWF changes spectral power in several ways (Fig. 15). First, the peak spectral density (at low frequency, low wavenumber) decreases by about 20%. Overall, spectral power is reduced with the removal of the EWF, although a curious wavenumber 6–7, approximately 15-day peak, appears. The wavenumber-1 peak is shifted from its EWF period of approximately 50 days to a period of about 80 days. Viewed from the power spectra, the effect of removing the EWF appears dramatic.

b. The effect of extratropical excitation

The suppression of extratropical excitation substantially decreases the magnitude of the zonal wind and OLR anomalies (Figs. 16 and 17, respectively) even more severely than with the removal of the EWF. For 250- and 850-hPa zonal wind, the degree of decrease is such that July–October anomalies are virtually eliminated. During May–June, some small-amplitude, eastward-propagating variability may still be seen at 250 hPa. In OLR, most anomalies are so reduced by the removal of extratropical excitation that they are almost not seen at the same contour interval as Fig. 3. Zonal wind phase speeds are roughly unchanged compared to the control run, perhaps with some slowing. For instance, in 250-hPa zonal wind, phase speed shows a pronounced slowing east of the date line from March to August.

When extratropical excitation is suppressed, the eastward-propagating signal in lower-level zonal wind spectral power (Figs. 18c,d) is severely reduced at low wavenumbers and intraseasonal frequencies. In upper-level zonal wind (Figs. 18a,b), the decrease in overall power is not as severe. While power for periods shorter than approximately 40 days at wavenumber 1 is almost eliminated, at around 80 days, wavenumber 1 retains about half of the peak power as compared to the control run. In OLR (Fig. 19), wavenumber-1 spectral power is roughly an order of magnitude smaller. The main peak for OLR spectra is at wavenumber 2, at a period of

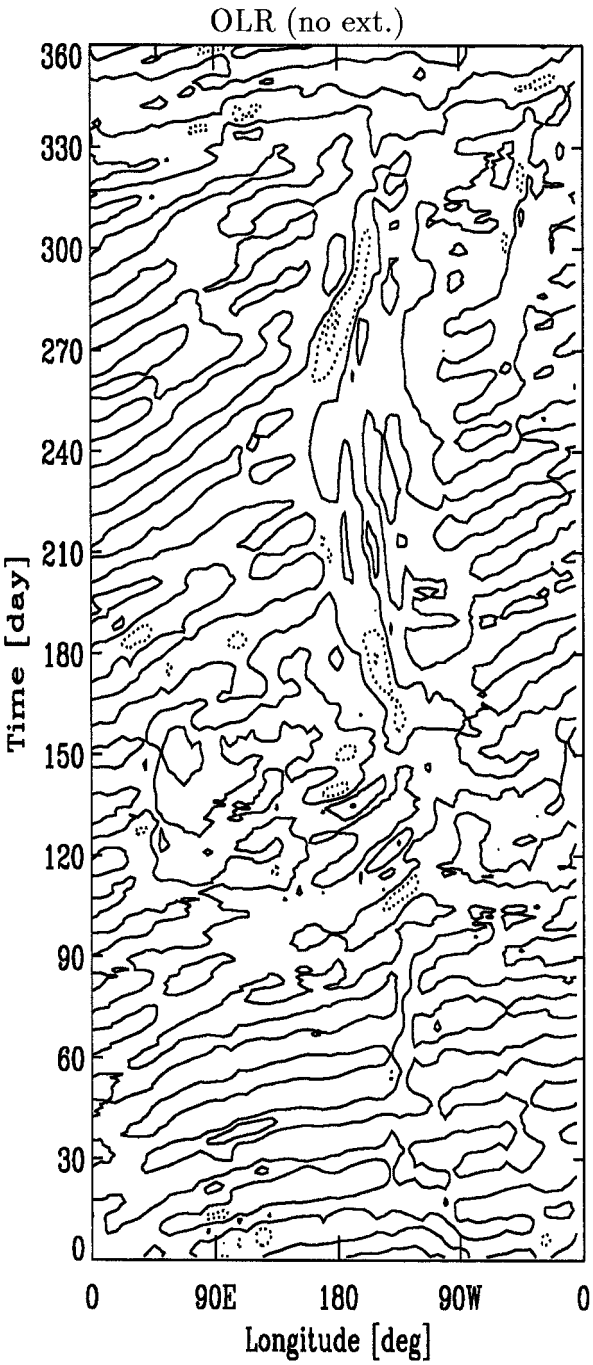

FIG. 17. As in Fig. 4, except for OLR anomaly (contour 5 W m^{-2}) for extratropical excitation is removed.

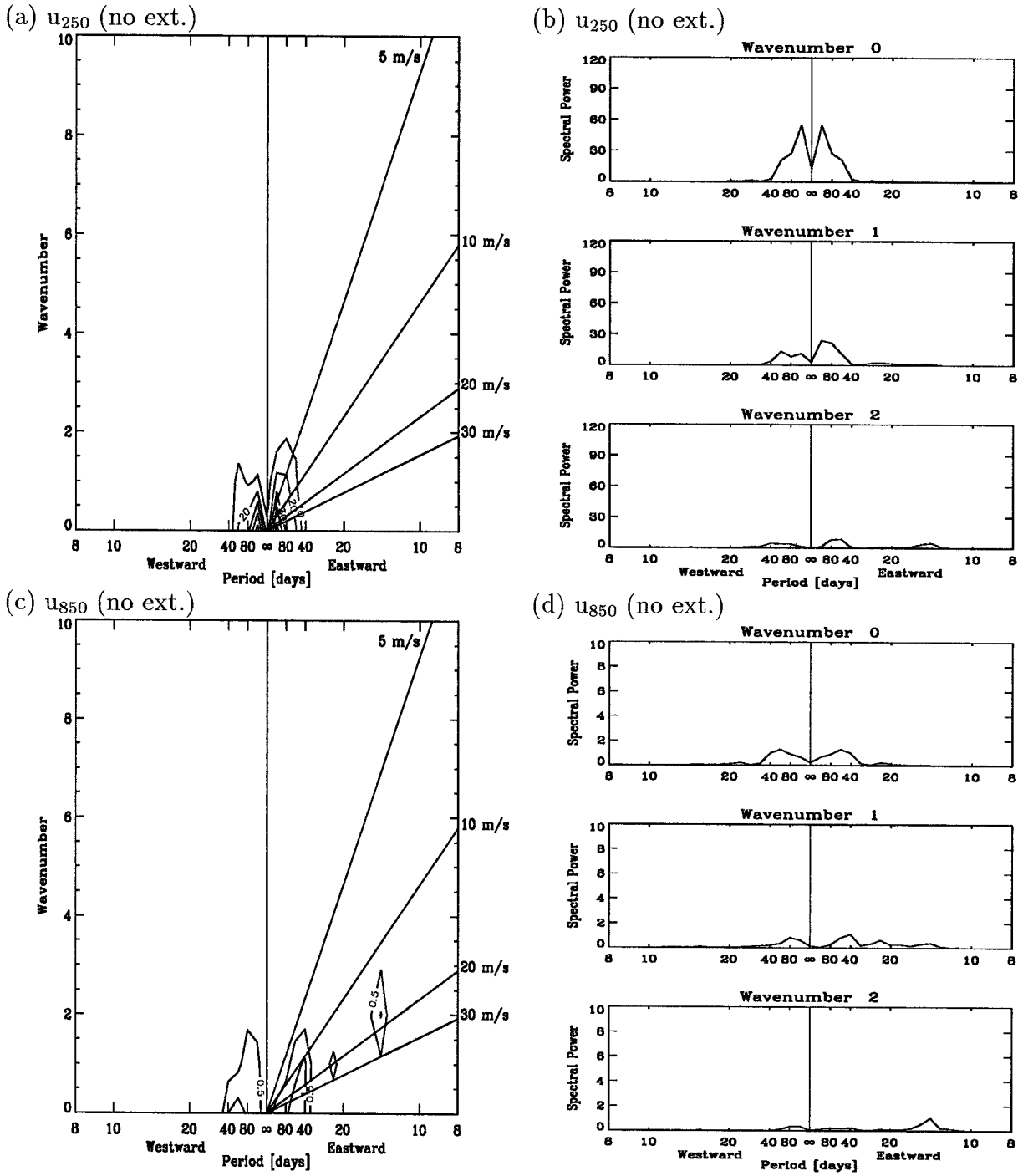

FIG. 18. As in Fig. 5, except extratropical excitation is removed. PSD as wavenumber-frequency contour plots and wavenumber 0–2 slices are shown. (a) an (b) 250-hPa zonal wind; and (c) and (d) 850-hPa zonal wind. Units of $(\text{m s}^{-1})^2$. Contour intervals are (a) 10 and (c) 0.5. Standard deviation of PSDs is 10%.

about 13 days. However, its magnitude is only about half that of the peak power for the control run.

Interestingly, the spectral power plots also show evidence of some other phenomena in both upper- and lower-level zonal winds at wavenumber 0, which remains even when extratropical excitation is removed. For lower-level zonal wind (Figs. 18c,d), wavenumber 0 retains about half of the power (at a period of 53 days) found when extratropical excitation is retained. With upper-level zonal wind (Figs. 18a,b), around half the

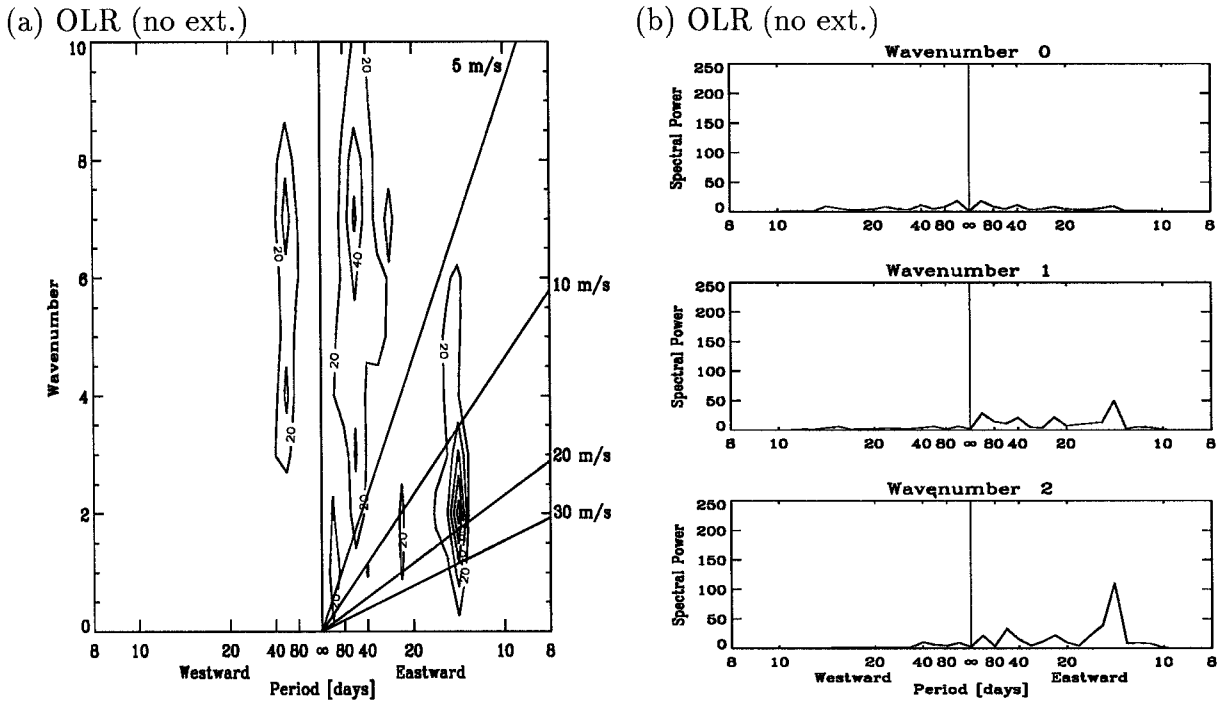

FIG. 19. As in Fig. 6, except PSD for extratropical excitation removed is shown. Units of $(W\ m^{-2})^2$. Contour interval for (a) is 20. Standard deviation of PSDs is 10%.

power is retained (at a period of about 160 days). This retention of wavenumber 0 power does not appear to hold true for OLR. Although the cause of this wavenumber-0 standing oscillation is unknown, one hypothesis is that it is associated with nonlinear symmetric instability (Zhao and Ghil 1991).

When both the EWF and extratropical excitation are removed, the equatorial zonal wind anomalies (Fig. 20) are suppressed even more than in either of the cases where only one mechanism is removed. For 850-hPa zonal wind, it becomes difficult to find a propagating signal in all months of the year. If the time–longitude plot uses a smaller contour interval (not shown), a small equatorial signal can be detected; however, it is sporadic in time and space (e.g., there is a signal between 60° and 120°E longitude, only during DJF). For 250-hPa zonal wind, some anomalies remain, most notably the slower phase speed disturbances east of the date line during April–June, though otherwise anomalies are small. Similarly, OLR anomalies (Fig. 21) also decrease in magnitude. The removal of the EWF and extratropical excitation also appears to decrease OLR phase speed even during DJF.

The removal of both the EWF and extratropical excitation produces upper- and lower-level zonal wind power spectral density similar to that for the case of removing only extratropical excitation for eastward-propagating components at wavenumber 1 (Fig. 22). For OLR (Fig. 23), spectral power is essentially removed at most wavenumbers and frequencies. The wavenumber-0 component of the upper-level zonal wind continues to retain noticeable spectral power. For the lower-level zonal wind, the spectral power at wavenumber 0 does not appear very important.

5. A hypothesis regarding the relationship of the MJO to the moist Kelvin wave

In the introduction (section 1b), we reviewed WK's discussion of possible distinctions between the MJO and the moist Kelvin wave. The main feature, as we read their plots, is that the peaks of enhanced PSD associated with each are the same or overlap at wavenumber 1, but the MJO peak extends across several wavenumbers in a fixed spectral band (30–60 days) while the moist Kelvin wave extends almost nondispersively to higher frequencies with wavenumber.

An analog to this behavior is apparently seen in this model (see Fig. 7 and discussion in section 3b). Since this model includes various physical processes (e.g., cloud radiative interactions, etc.), it is possible that the MJO-like variance in this model could be a distinct phenomena maintained by different processes from the moist Kelvin wave. However, we find in our experiments that both tend to be suppressed at the same time when midlatitude variability is artificially suppressed. To explain the WK-type distinction between the moist Kelvin wave and the MJO, at least in this model, we hypothesize that the spread of variance at MJO frequencies across various wavenumbers is due to inter-

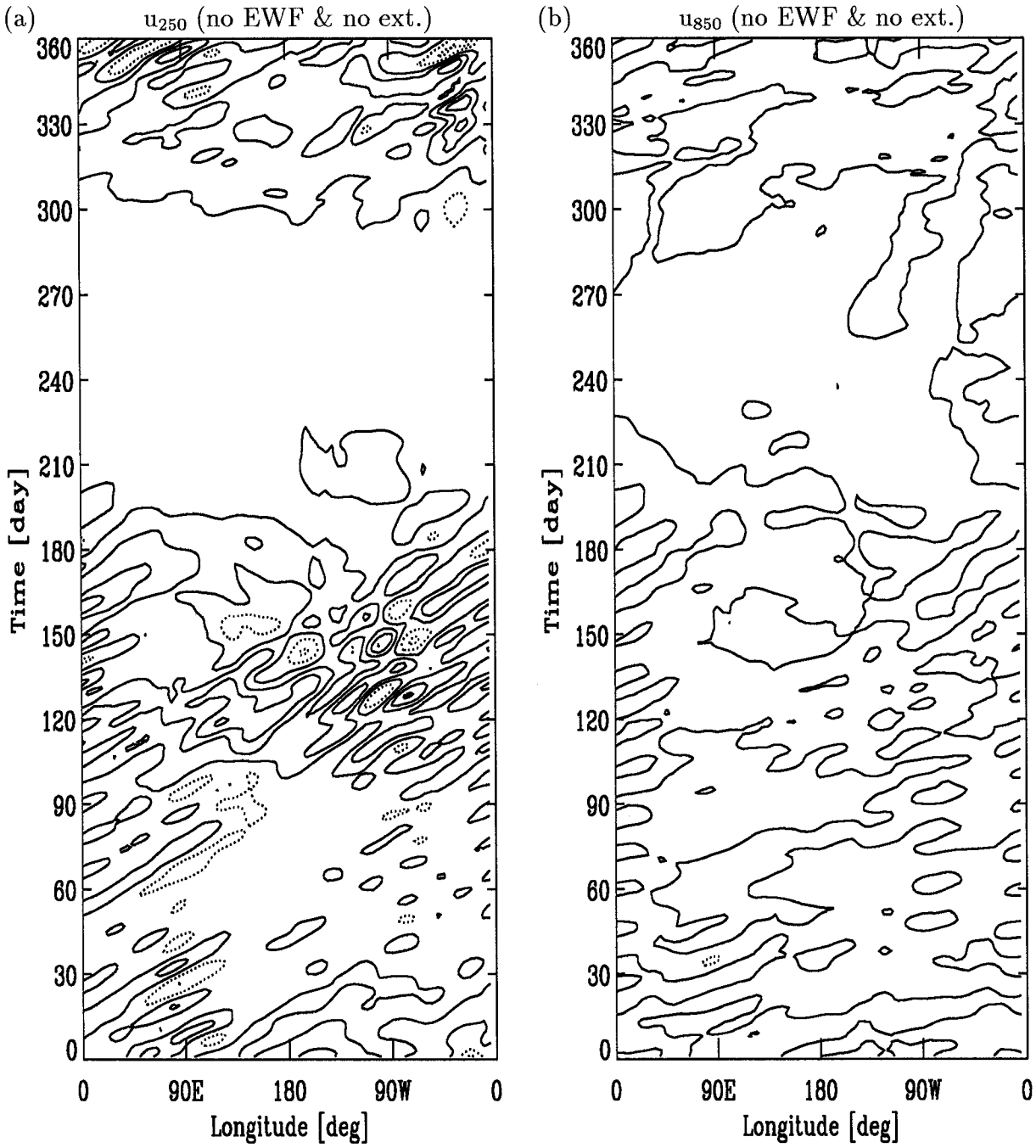

FIG. 20. As in Fig. 3, except both the EWF and extratropical excitation are removed. Zonal wind anomaly is shown at (a) 250 hPa (contour 1 m s^{-1}) and (b) 850 hPa (contour 0.5 m s^{-1}).

action of the wavenumber-1 moist Kelvin wave with a zonally asymmetric basic state. Majda et al. (1999) have examined such interactions of a Kelvin wave with a stationary forcing to produce other zonal wavenumbers and other equatorial wavetypes in nonlinear shallow-water equations interacting with topography. Analogous features would apply in the moist-convective case.

To illustrate such interactions in a linearized context, with perturbation and basic state quantities x' and $\overline{x}$, consider for example the convection formulation in our model, which has terms such as $C'\mathcal{H}(\overline{C})$, where C is CAPE and $\mathcal{H}$ is the Heaviside function. If the basic state is not zonally uniform, one can write $\mathcal{H}(\overline{C}) = H_0 + \Sigma_n H_n e^{inx}$ + complex conjugate, where n is the zonal wavenumber. Consider a wave initially of the form $C' = Ae^{i(mx-\omega t)}$ + complex conjugate, where m is the zonal

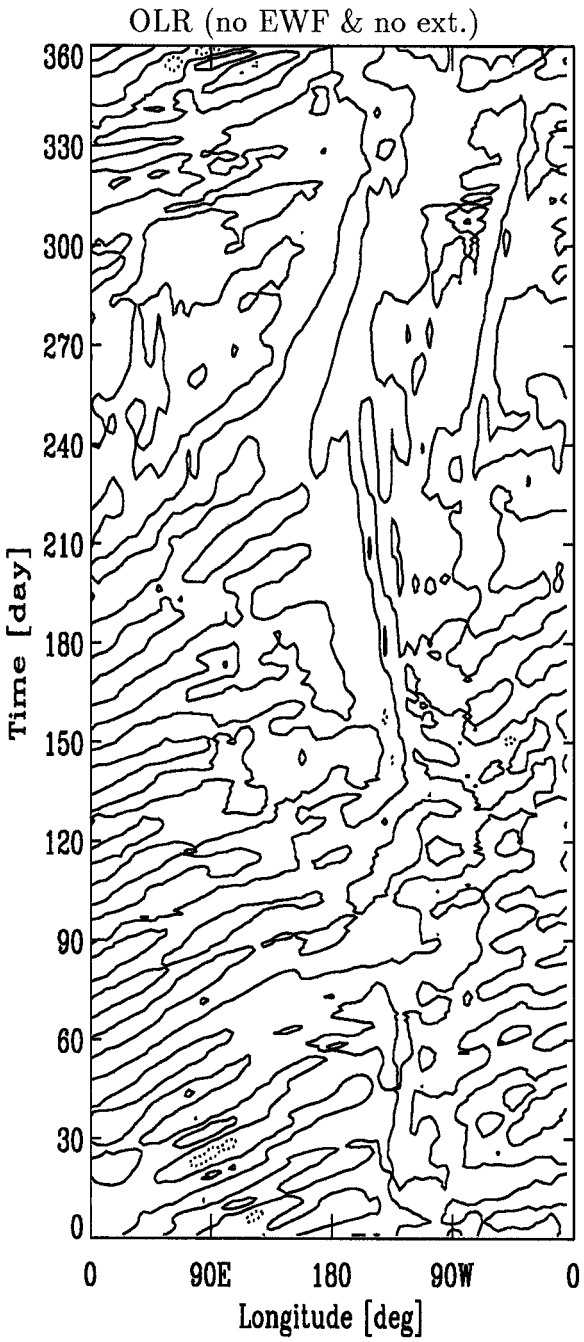

FIG. 21. As in Fig. 4, except for OLR anomaly (contour 5 W m^{-2}) both the EWF and extratropical excitation are removed.

wavenumber, A is an amplitude, and ω is the frequency. Interactions of the wave with the zonally asymmetric basic state, such as $C'\mathcal{H}(\overline{C})$, will produce power at wavenumbers $\pm m \pm n$ for all n, but at the original frequency ω. Power that tends to occur at 30–60 days at wavenumber 1 in the wave will thus spread in this spectral band across higher wavenumbers. Nonlinear interaction of the time-dependent wave with itself would generate other frequencies, so interaction with the basic state is most relevant to the wavenumber spread at constant frequency. Complications involving matching of meridional structures necessarily occur, since for power that gets spread to negative zonal wavenumbers at low frequencies, the match to Rossby wave dynamics must be taken into account (Majda et al. 1999).

We caution that we have not shown that this hypothesized mechanism is responsible for the moist-Kelvin wave/MJO-like distinction in this model. The importance of this mechanism relative to others in observations is even less clear, but the mechanism is simple, so we suggest it as a starting point against which more elaborate hypothesis may be compared.

6. Discussion and conclusions

From these numerical experiments, a few conclusions can be drawn regarding the mechanisms involved in maintaining intraseasonal oscillations in an atmospheric model of intermediate complexity. These are suggestive of mechanisms that may operate in real-world intraseasonal oscillations and also serve as examples for examining the difficulties faced by diagnostic techniques in attempting to sort out mechanisms in observations. First, these results are consistent with the view of the intraseasonal oscillations (described in section 1b) as being associated with intrinsic CID modes of the tropical atmosphere that are maintained against damping by some input of energy. The form and phase speed of the model eastward-propagating disturbances are more complex than in linearized studies of a related model (Neelin and Yu 1994; Yu and Neelin 1994). The eastward propagation and spatial form are recognizably related to the Kelvin–CID mode of the linear case, although differences may be noted. CISK (in the sense of instability) is known not to occur in the linear case, and this carries over to this model, since the oscillation disappears when other mechanisms are suppressed. A linear analysis of this model does appear to give a qualitative explanation of phase speed variations with season. These are mainly due to the effects of advection by the mean wind, which substantially slows the propagation in some seasons.

The model has an analog of the frequency-wavenumber signature noted in observations by Wheeler and Kiladis (1999) in which spectral enhancement relative to background occurs in both a curve suggestive of a moist Kelvin wave and as low-frequency peaks extending from the dominant wavenumber 1 out to wavenumber 6 at constant frequency. In the model, both are maintained by similar mechanisms, so when we refer to both aspects, we use the term ''moist-Kelvin/MJO-like'' variance. This is not intended to imply that they are necessarily related. We use the term intraseasonal variance to refer to all the variability at intraseasonal timescales, including the moist-Kelvin/MJO-like variance.

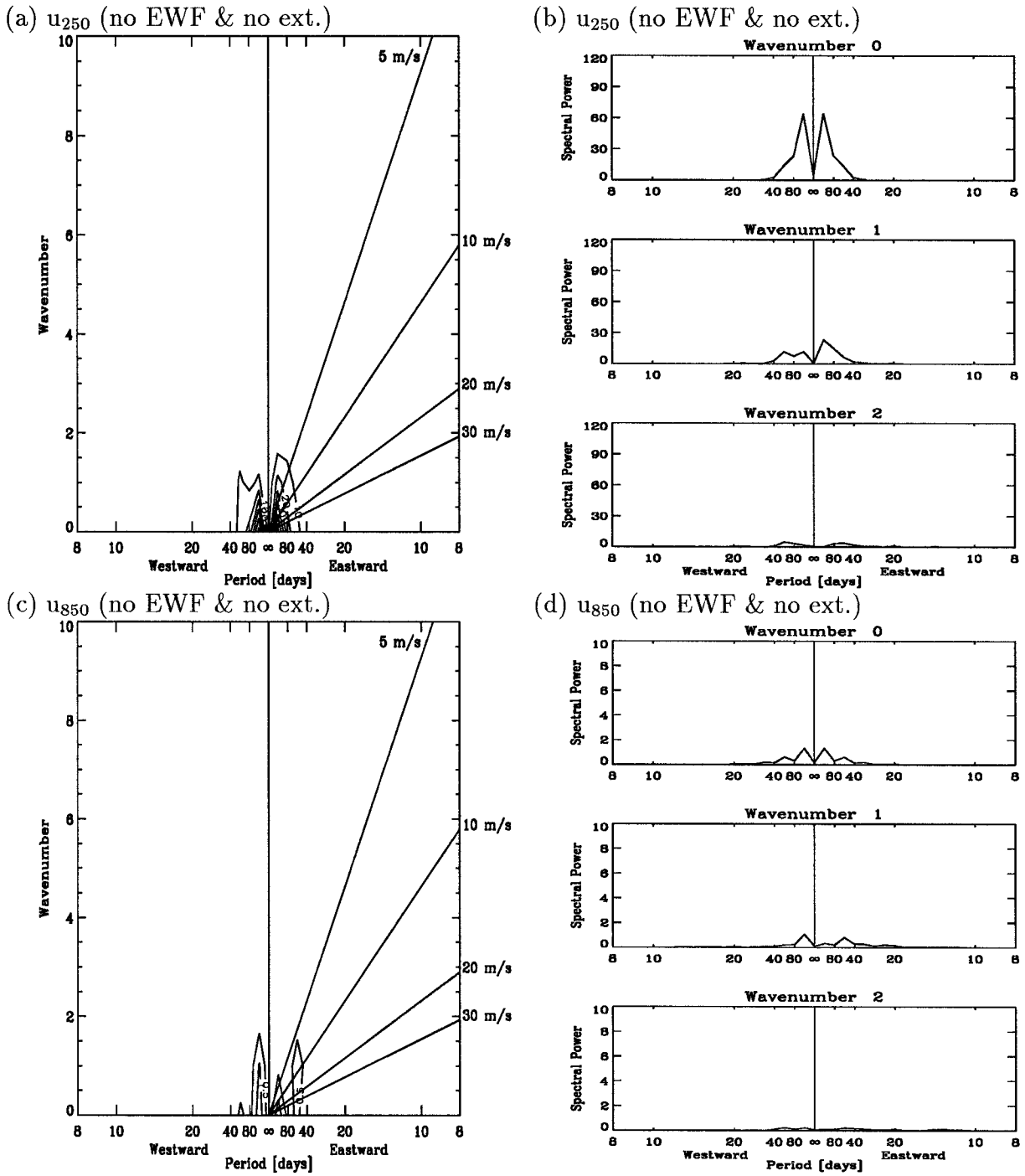

FIG. 22. As in Fig. 5, except both the EWF and extratropical excitation are removed. PSD as wavenumber–frequency contour plots and wavenumber 0–2 slices are shown. (a) and (b) 250-hPa zonal wind; (c) and (d) 850-hPa zonal wind. Units of $(\text{m s}^{-1})^2$. Contour intervals are (a) 10 and (c) 0.5. Standard deviation of PSDs is 10%.

The experiments presented in this paper suggest that both the EWF and extratropical excitation can act to maintain intraseasonal variance. If either of the mechanisms is removed, the model simulated oscillation is reduced. Of the two mechanisms, the removal of extratropical excitation decreases the amplitude of the variance more than removing the EWF. Although both mechanisms appear necessary for the maintenance of the moist-Kelvin/MJO-like oscillation, each mechanism appears to influence the oscillation differently. The EWF, if acting alone without extratropical excitation, does not appear able to maintain the oscillation. Neither

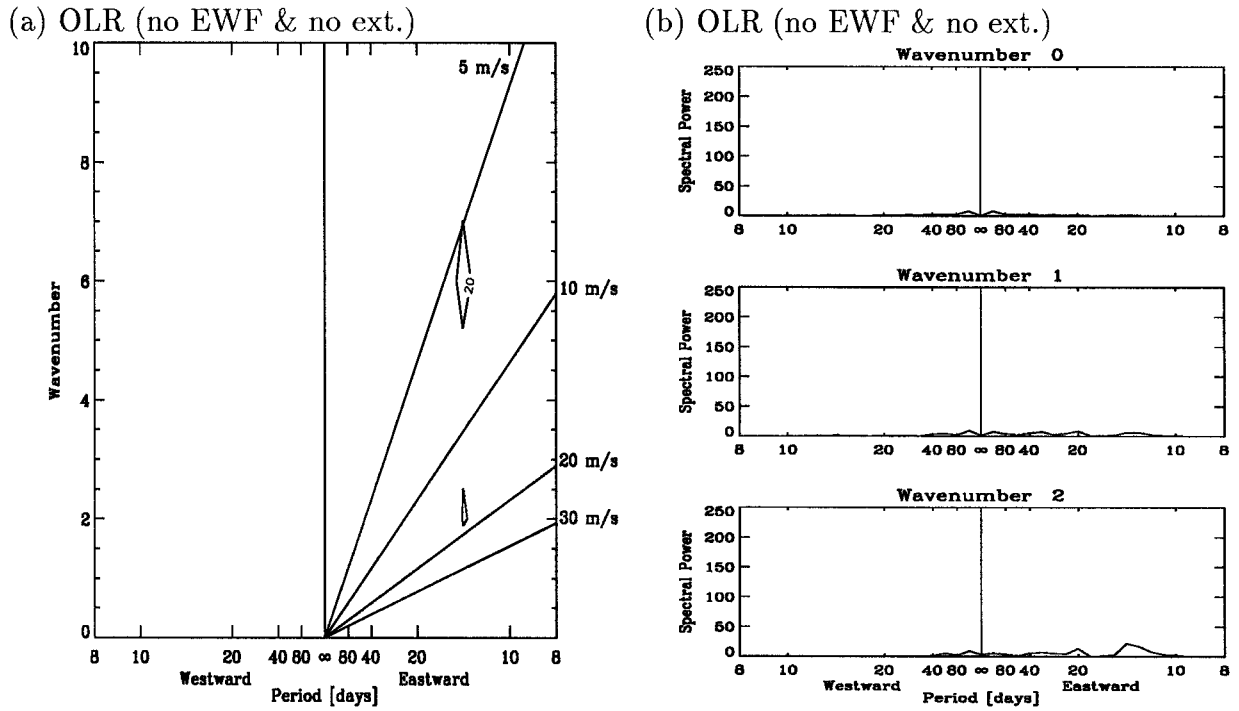

FIG. 23. As in Fig. 6, except PSD for both the EWF and extratropical excitation removed is shown. Units of $(W\ m^{-2})^2$. Contour interval for (a) is 20. Standard deviation of PSDs is 10%.

can the extratropical excitation if acting alone, although in the case of extratropical excitation acting without the EWF, one sees evidence of regions (localized in space and time) where eastward propagation continues. The main spectral feature maintained by extratropical excitation acting alone seems not to be related to moist-Kelvin/MJO-like variance, since its wavenumber-1 component has a peak period of about 160 days. We underline the caveat that the midlatitude storms in this model are not as accurately represented as tropical aspects and that the midlatitude variance and the extension of storms into the Tropics can be sensitive to model parameters (ZNC). Results from a more recent version of the model (v2.1 ZNC), in which the intensity of midlatitude storms is less than those simulated in the version used for this study (v1.0), show a marked decrease in intraseasonal variability. Thus, we regard the results of this study as an illustration of midlatitude impacts, showing what the midlatitudes could do under some circumstances, rather than a quantitative estimate.

Although the numerical experiments presented in this study indicate that the EWF helps maintain moist-Kelvin/MJO-like variance, analysis of the evaporation signal in the model oscillation suggests the current prototypes for wind–evaporation interaction are inadequate to fully describe the feedback. Both the zonally inhomogeneous basic state and the more complex model oscillation structure appear to impact this. If so, there is the potential for drawing misleading conclusions regarding wind–evaporation interaction from the current observational studies. Determining the importance or nonimportance of the EWF will require the use of numerical experiments, such as those used in this study, or better theoretical prototypes to guide analysis.

The results presented here also allow some comments to be made with respect to other proposed mechanisms for maintaining intraseasonal oscillations. First, this study demonstrates that a moist-Kelvin/MJO-like oscillation can be sustained in an intermediate-level atmospheric model without CISK instability, implying other mechanisms can maintain such an oscillation. In addition, the impact of ''noise'' from extratropical excitation suggests that other types of noise may have an influence in maintaining intraseasonal oscillations. Possible sources of noise include convective-scale activity and mesoscale disturbances, whose variances are unresolved by traditional convective parameterizations (including the Betts–Miller scheme used in the QTCM1) that calculate ensemble means at model grid points.

In summary, these results suggest the following, at least in this model.

- The EWF (a) does not alone maintain the moist-Kelvin/MJO-like oscillations by producing instability but assists midlatitude excitation by reducing decay and (b) can favor intraseasonal variance at MJO-like periods (approximately 20–80 days in this model) and low wavenumbers.
- Extratropical excitation (a) can provide a source of stochastic excitation to sustain intraseasonal variance

and (b) in the absence of the EWF, still creates tropical intraseasonal variability but not the peak response at the periods of the model's moist Kelvin and MJO-like modes.

- In the relationship between moist Kelvin and MJO-like variability, the maintenance mechanisms for both these aspects of the model variability are related. Although not confirmed here, it is conjectured that nonlinear effects may generate the higher wavenumber aspects of the MJO-like feature from the wavenumber-1 moist Kelvin wave.

A preliminary analysis of the pathway by which extratropical excitation influences the Tropics suggests that it is not simple to distinguish among several possible mechanisms. These include Rossby wave propagation as described in Hsu et al. (1990), the effect of baroclinic waves sweeping through the Tropics upon divergence, or the effect of these on moisture advection. While determining which is dominant will require additional study, this paper demonstrates a clean method of suppressing midlatitude disturbances that can be used in other models and provides a clear example of a case where midlatitude effects are shown to be important.

Acknowledgments. This research was partially supported by National Science Foundation Grant ATM-9521389 and National Oceanic and Atmospheric Administration Grant NA86GP0314. This study benefited from comments from an anonymous reviewer and discussions with B. Chen, J. Gao, H. Hendon, C. Lin, A. Majda, D. Porinchu, H. Su, W. Tung, M. Wheeler, M. Yanai, and especially C. Chou.

REFERENCES

Anyamba, E. K., and B. C. Weare, 1995: Temporal variability of the 40–50 day oscillation in tropical convection. *Int. J. Climatol.,* **15,** 379–402.

Betts, A. K., 1982: Saturation point analysis of moist convective overturning. *J. Atmos. Sci.,* **39,** 1484–1505.

——, and M. J. Miller, 1986: A new convective adjustment scheme. Part II: Single column tests using GATE wave, BOMEX, ATEX and arctic air-mass data sets. *Quart. J. Roy. Meteor. Soc.,* **112,** 693–709.

Bladé, I., and D. L. Hartmann, 1993: Tropical intraseasonal oscillations in a simple nonlinear model. *J. Atmos. Sci.,* **50,** 2922–2939.

Brooks, C. E. P., and N. Carruthers, 1953: *Handbook of Statistical Methods in Meteorology.* Her Majesty's Stationery Office, 412 pp.

Brown, R. G., and C. S. Bretherton, 1995: Tropical wave instabilities: Convective interaction with dynamics using the Emanuel convective parameterization. *J. Atmos. Sci.,* **52,** 67–82.

Chang, C.-P., 1977: Viscous internal gravity waves and low-frequency oscillations in the tropics. *J. Atmos. Sci.,* **34,** 901–910.

——, and H. Lim, 1988: Kelvin wave-CISK: A possible mechanism for the 30–50 day oscillations. *J. Atmos. Sci.,* **45,** 1709–1720.

Charney, J. G., and A. Eliassen, 1964: On the growth of the hurricane depression. *J. Atmos. Sci.,* **21,** 68–74.

Crum, F. X., and T. J. Dunkerton, 1992: Analytic and numerical models of wave-CISK with conditional heating. *J. Atmos. Sci.,* **49,** 1693–1708.

——, and ——, 1994: CISK and evaporation-wind feedback with conditional heating on an equatorial beta-plane. *J. Meteor. Soc. Japan,* **72,** 11–18.

Dunkerton, T. J., and F. X. Crum, 1995: Eastward propagating ~2- to 15-day equatorial convection and its relation to the tropical intraseasonal oscillation. *J. Geophys. Res.,* **100,** 25 781–25 790.

Emanuel, K. A., 1987: An air–sea interaction model of intraseasonal oscillations in the tropics. *J. Atmos. Sci.,* **44,** 2324–2340.

——, 1988: Reply. *J. Atmos. Sci.,* **45,** 3528–3530.

——, J. D. Neelin, and C. S. Bretherton, 1994: On large-scale circulations in convecting atmospheres. *Quart. J. Roy. Meteor. Soc.,* **120,** 1111–1143.

Ferranti, L., T. N. Palmer, F. Molteni, and E. Klinker, 1990: Tropical–extratropical interaction associated with the 30–60 day oscillation and its impact on medium and extended range prediction. *J. Atmos. Sci.,* **47,** 2177–2199.

Gill, A. E., 1980: Some simple solutions for heat-induced tropical circulation. *Quart. J. Roy. Meteor. Soc.,* **106,** 447–462.

Gruber, A., 1974: Wavenumber-frequency spectra of satellite-measured brightness in tropics. *J. Atmos. Sci.,* **31,** 1675–1680.

Hayashi, Y., 1971: Large-scale equatorial waves destabilized by convective heating in the presence of surface friction. *J. Meteor. Soc. Japan,* **49,** 458–466.

——, and D. G. Golder, 1986: Tropical intraseasonal oscillations appearing in a GFDL general circulation model and FGGE data. Part I: Phase propagation. *J. Atmos. Sci.,* **43,** 3058–3067.

——, and A. Sumi, 1986: The 30–40 day oscillations simulated in an ''aqua planet'' model. *J. Meteor. Soc. Japan,* **64,** 451–467.

——, and S. Miyahara, 1987: A three-dimensional linear response model of the tropical intraseasonal oscillation. *J. Meteor. Soc. Japan,* **65,** 843–852.

——, and D. G. Golder, 1997: United mechanisms for the generation of low- and high-frequency tropical waves. Part I: Control experiments with moist convective adjustment. *J. Atmos. Sci.,* **54,** 1262–1276.

Hendon, H. H., 1988: A simple model of the 40–50 day oscillation. *J. Atmos. Sci.,* **45,** 569–584.

——, and B. Liebmann, 1994: Organization of convection within the Madden–Julian oscillation. *J. Geophys. Res.,* **99,** 8073–8083.

——, and M. L. Salby, 1994: The life cycle of the Madden–Julian oscillation. *J. Atmos. Sci.,* **51,** 2225–2237.

——, and J. Glick, 1997: Intraseasonal air–sea interaction in the tropical Indian and Pacific Oceans. *J. Climate,* **10,** 647–661.

Hsu, H.-H., B. J. Hoskins, and F.-F. Jin, 1990: The 1985/86 intraseasonal oscillation and the role of the extratropics. *J. Atmos. Sci.,* **47,** 823–839.

Hu, Q., and D. A. Randall, 1994: Low-frequency oscillations in radiative–convective systems. *J. Atmos. Sci.,* **51,** 1089–1099.

Itoh, H., and N. Nishi, 1990: Considerations for the structure of the tropical intraseasonal oscillation. *J. Meteor. Soc. Japan,* **68,** 659–675.

Jones, C., and B. C. Weare, 1996: The role of low-level moisture convergence and ocean latent heat fluxes in the Madden and Julian oscillation: An observational analysis using ISCCP data and ECMWF analyses. *J. Climate,* **9,** 3086–3104.

Knutson, T. R., and K. M. Weickmann, 1987: 30–60 day atmospheric oscillations: Composite life cycles of convection and circulation anomalies. *Mon. Wea. Rev.,* **115,** 1407–1436.

Lau, K.-M., and P. H. Chan, 1985: Aspects of the 40–50 day oscillation during the northern winter as inferred from outgoing longwave radiation. *Mon. Wea. Rev.,* **113,** 1889–1909.

——, and L. Peng, 1987: Origin of low-frequency (intraseasonal) oscillations in the tropical atmosphere. Part I: Basic theory. *J. Atmos. Sci.,* **44,** 950–972.

——, I. M. Held, and J. D. Neelin, 1988: The Madden–Julian oscillation in an idealized general circulation model. *J. Atmos. Sci.,* **45,** 3810–3832.

Liebmann, B., and D. L. Hartmann, 1984: An observational study of tropical–midlatitude interaction on intraseasonal time scales during winter. *J. Atmos. Sci.,* **41,** 3333–3350.

Lim, H., T.-K. Lim, and C.-P. Chang, 1990: Reexamination of wave-CISK theory: Existence and properties of nonlinear wave-CISK modes. *J. Atmos. Sci.,* **47,** 3078–3091.

Lindzen, R. S., 1974: Wave-CISK in the tropics. *J. Atmos. Sci.,* **31,** 156–179.

Livezey, R. E., and W. Y. Chen, 1983: Statistical field significance and its determination by Monte Carlo techniques. *Mon. Wea. Rev.,* **111,** 46–59.

Madden, R. A., and P. R. Julian, 1971: Detection of a 40–50 day oscillation in the zonal wind in the tropical Pacific. *J. Atmos. Sci.,* **28,** 702–708.

——, and ——, 1972: Description of global-scale circulation cells in the tropics with a 40–50 day period. *J. Atmos. Sci.,* **29,** 1109–1123.

——, and ——, 1994: Observations of the 40-50-day tropical oscillation—A review. *Mon. Wea. Rev.,* **122,** 814–837.

Majda, A. J., R. R. Rosales, E. G. Tabak, and C. V. Turner, 1999: Interaction of large-scale equatorial waves and dispersion of Kelvin waves through topographic resonances. *J. Atmos. Sci.,* **56,** 4118–4133.

Matsuno, T., 1966: Quasi-geostrophic motions in the equatorial area. *J. Meteor. Soc. Japan,* **44,** 25–43.

Meehl, G. A., G. N. Kiladis, K. M. Weickmann, M. Wheeler, D. S. Gutzler, and G. P. Compo, 1996: Modulation of equatorial subseasonal convective episodes by tropical–extratropical interaction in the Indian and Pacific Ocean regions. *J. Geophys. Res.,* **101,** 15 033–15 049.

Milliff, R. F., and R. A. Madden, 1996: The existence and vertical structure of fast, eastward-moving disturbances in the equatorial troposphere. *J. Atmos. Sci.,* **53,** 586–597.

Murakami, M., 1984: Analysis of the deep convective activity over the Western Pacific and Southeast Asia. Part II: Seasonal and intraseasonal variations during Northern Summer. *J. Meteor. Soc. Japan,* **62,** 88–108.

Neelin, J. D., 1997: Implications of convective quasi-equilibrium for the large-scale flow. *The Physics and Parameterization of Moist Convection,* Kluwer Academic, 413–446.

——, and J.-Y. Yu, 1994: Modes of tropical variability under convective adjustment and the Madden–Julian oscillation. Part I: Analytical theory. *J. Atmos. Sci.,* **51,** 1876–1894.

——, and N. Zeng, 2000: A quasi-equilibrium tropical circulation model—Formulation. *J. Atmos. Sci.,* **57,** 1741–1766.

——, I. M. Held, and K. H. Cook, 1987: Evaporation-wind feedback and low-frequency variability in the tropical atmosphere. *J. Atmos. Sci.,* **44,** 2341–2348.

Numaguti, A., and Y.-Y. Hayashi, 1991: Behavior of cumulus activity and the structures of circulations in an ''aqua planet'' model. Part II: Eastward-moving planetary scale structure and the intertropical convergence zone. *J. Meteor. Soc. Japan,* **69,** 563–579.

Ooyama, K., 1964: A dynamical model for the study of tropical cyclone development. *Geofis. Int.,* **4,** 187–198.

Press, W. H., B. P. Flannery, S. A. Teukolsky, and W. T. Vetterling, 1989: *Numerical Recipes in Pascal*. Cambridge University Press, 750 pp.

Randall, D. A., and J. Wang, 1992: The moist available energy of a conditionally unstable atmosphere. *J. Atmos. Sci.,* **49,** 240–255.

Reynolds, R. W., 1988: A real-time global sea surface temperature analysis. *J. Climate,* **1,** 75–86.

Salby, M. L., and R. R. Garcia, 1987: Transient response to localized episodic heating in the tropics. Part I: Excitation and short-time near-field behavior. *J. Atmos. Sci.,* **44,** 458–498.

——, and H. H. Hendon, 1994: Intraseasonal behavior of clouds, temperature, and motion in the Tropics. *J. Atmos. Sci.,* **51,** 2207–2224.

——, R. R. Garcia, and H. H. Hendon, 1994: Planetary-scale circulations in the presence of climatological and wave-induced heating. *J. Atmos. Sci.,* **51,** 2344–2367.

Seager, R., and S. E. Zebiak, 1994: Convective interaction with dynamics in a linear primitive equation model. *J. Atmos. Sci.,* **51,** 1307–1331.

Slingo, J. M., 1998: Extratropical forcing of tropical convection in a northern winter simulation with the UGAMP GCM. *Quart. J. Roy. Meteor. Soc.,* **124,** 27–51.

——, and Coauthors, 1996: Intraseasonal oscillations in 15 atmospheric general circulation models: Results from an AMIP diagnostic subproject. *Climate Dyn.,* **12,** 325–357.

Sperber, K. R., J. M. Slingo, P. M. Inness, and W. K.-M. Lau, 1997: On the maintenance and initiation of the intraseasonal oscillation in the NCEP/NCAR reanalysis and in the GLA and UKMO AMIP simulation. *Climate Dyn.,* **13,** 769–795.

Swinbank, R., T. N. Palmer, and M. K. Davey, 1988: Numerical simulations of the Madden and Julian oscillation. *J. Atmos. Sci.,* **45,** 774–788.

Takayabu, Y. N., 1994: Large-scale cloud disturbances associated with equatorial waves. Part I: Spectral features of the cloud disturbances. *J. Meteor. Soc. Japan,* **72,** 433–449.

Waliser, D. E., K. M. Lau, and J.-H. Kim, 1999: The influence of coupled sea surface temperatures on the Madden–Julian oscillation: A model perturbation experiment. *J. Atmos. Sci.,* **56,** 333–358.

Wang, B., 1988: Comments on ''An air–sea interaction model of intraseasonal oscillation in the tropics.'' *J. Atmos. Sci.,* **45,** 3521–3525.

——, and H. Rui, 1990: Synoptic climatology of transient tropical intraseasonal convection anomalies. *Meteor. Atmos. Phys.,* **44,** 43–61.

——, and X. Xie, 1998: Coupled modes of the warm pool climate system. Part I: The role of air–sea interaction in maintaining Madden–Julian oscillation. *J. Climate,* **11,** 2116–2135.

Weickmann, K. M., G. R. Lussky, and J. E. Kutzbach, 1985: Intraseasonal (30–60 day) flucutations of outgoing longwave radiation and 250 mb streamfunction during northern winter. *Mon. Wea. Rev.,* **113,** 941–961.

Wheeler, M., and G. N. Kiladis, 1999: Convectively coupled equatorial waves: Analysis of clouds and temperature in the wavenumber-frequency domain. *J. Atmos. Sci.,* **56,** 374–399.

Xie, S.-P., A. Kubokawa, and K. Hanawa, 1993: Evaporation-wind feedback and the organizing of tropical convection on the planetary scale. Part I: Quasi-linear instability. *J. Atmos. Sci.,* **50,** 3873–3883.

Xu, K.-M., and K. A. Emanuel, 1989: Is the tropical atmosphere conditionally unstable? *Mon. Wea. Rev.,* **117,** 1471–1479.

Yanai, M., B. Chen, and W.-W. Tung, 2000: The Madden–Julian oscillation observed during the TOGA COARE IOP: Global view. *J. Atmos. Sci.,* **57,** 2374–2396.

Yu, J.-Y., and J. D. Neelin, 1994: Modes of tropical variability under convective adjustment and the Madden–Julian oscillation. Part II: Numerical results. *J. Atmos. Sci.,* **51,** 1895–1914.

Zeng, N., J. D. Neelin, and C. Chou, 2000: A quasi-equilibrium tropical circulation model—Implementation and simulation. *J. Atmos. Sci.,* **57,** 1767–1796.

Zhang, C., and H. H. Hendon, 1997: Propagating and standing components of the intraseasonal oscillation in tropical convection. *J. Atmos. Sci.,* **54,** 741–752.

Zhao, J.-X., and M. Ghil, 1991: Nonlinear symmetric instability and intraseasonal oscillations in the tropical atmosphere. *J. Atmos. Sci.,* **48,** 2552–2568.